ALMA MATER STUDIORUM - UNIVERSITÀ DI BOLOGNA

SCUOLA DI INGEGNERIA E ARCHITETTURA

DEI-Dipartimento dell'energia elettrica
e dell'informazione "Guglielmo Marconi"

Degree in Automation Engineering
AlmaTong project

TESI DI LAUREA

in
Laboratory of electric drives

Design of an AC inductor for phase shifted zero voltage switching converter

CANDIDATO
Francesco Taurone

RELATORE:
Chiar.mo Prof. Claudio Rossi

CORRELATORE
Ing. Matteo Marano

Anno Accademico 2015/16

To my family,
which supported me.

Contents

Introduction

English:

This thesis project is aimed to continue the development of a battery charger for automotive purposes. More specifically, after a general introduction of the charger itself, the thesis focuses on the AC inductor and its design, concluding with the results achieved. Due to the objectives for this design, most of the effort has been directed toward the limitation of losses, and therefore to efficiency improvement. The softwares needed for the following are Femm, Autocad 2010, Excel, Ferroxcube software and Matlab: the complementary use of the first four has been mainly employed for choosing and simulating the inductors, whereas the last one for the data analysis. After the test period in LEMAD Laboratory at University of Bologna, the designed inductor has been chosen as possible candidate to be installed on the charger. The overall system will be subjected to validations before the installation on vehicles.

Italiano:

Questo progetto di tesi è finalizzato al proseguimento dello sviluppo di un caricabatterie per applicazioni automotive. Nello specifico, dopo un' introduzione generale riguardo il funzionamento del caricatore, la tesi si focalizza sull'induttore AC e il suo corrispondente design, concludendo con i risultati ottenuti. A conseguenza degli obiettivi di questo design, particolare attenzione è stata diretta verso la limitazione di perdite, e conseguentemente verso un miglioramente dell'efficienza del sistema nella sua globalità. I software impiegati sono Femm, Autocad 2010, Excel, Ferroxcube software e Matlab: l'uso abbinato dei primi quattro è stato votato ai fini della scelta e della simulazione degli induttori, mentre l'ultimo ha permesso l'analisi dei dati raccolti. Dopo il periodo di test presso il laboratorio LEMAD dell'Università di Bologna, l'induttore risultato vincente dalle analisi del presente progetto è stato selezionato come possibile candidato per essere installato sul caricatore. Il sistema nel suo complesso verrà sottoposto a validazione prima dell'effettivo montaggio su veicolo.

Chapter 1

The charger

The charger basic structure consists of an insulated DC/DC converter working at a chosen frequency of 100kHz, with modules for rectification and inversion.
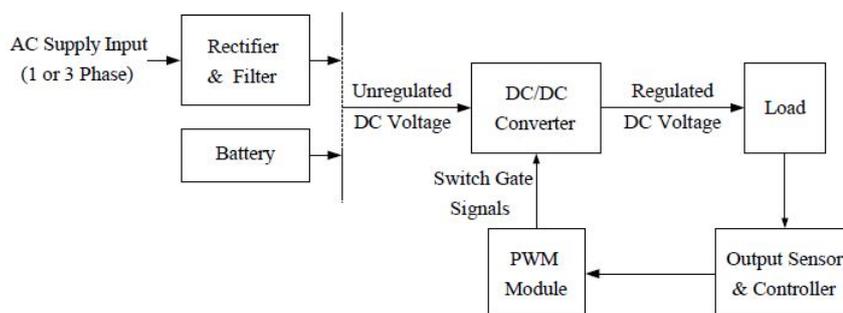

Figure 1.1: Basic scheme of the charger

Due to its working environment as automotive application, this design is bounded to performances enhancement and losses limitation, so to be both commercially competitive as performing charger and compliant with the strict regulation about this sector. As far as the following project is concerned, the main burden is the temperature increase, that must be limited: along with other techniques such as fins or fans for an increased dissipation capability, this thesis focus on limitation of losses pursuing the finest design as possible. Moreover, the charger is meant to be installed inside a waterproof box, making heat dissipation an even harder task.

Some techniques have been adopted in order to fulfill the design specifications, in terms of efficiency and energy transmission.

First of all, this **Switching Mode Power Source** utilizes a Soft **Zero Voltage Switching** Technique by means of *phase shifting* for limiting cyclic losses at inverter and rectifier level. Secondly, **Clamping Diodes** for reducing current peaks during the cycle. Further details will be part of the next chapters. Beside these, recent construction technologies allowed the use of multi-layers PCB for realizing transformer and inductances, which per-

mits up to a + 50% in heating dissipation with respect to standard typologies. However, the main target of this thesis is to present an alternative and more classic solution to this rather technologically advanced planar inductor, able to provide the charger with the same inductance for achieving ZVS, but with less losses. Reasons and proofs of this will be reported in the following, with practical examples.
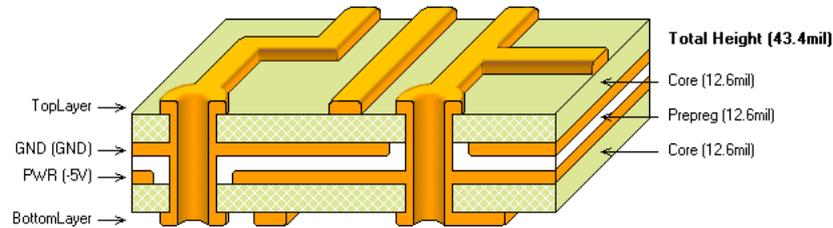
Figure 1.2: Example of layer stack

In order to understand the importance of the components designed within this thesis, a brief description of the phase shifted full bridge converter is reported, for the achievement of ZVS.

1.1 The Full-Bridge Phase-Shifted Zero Voltage Switching DC/DC Converter
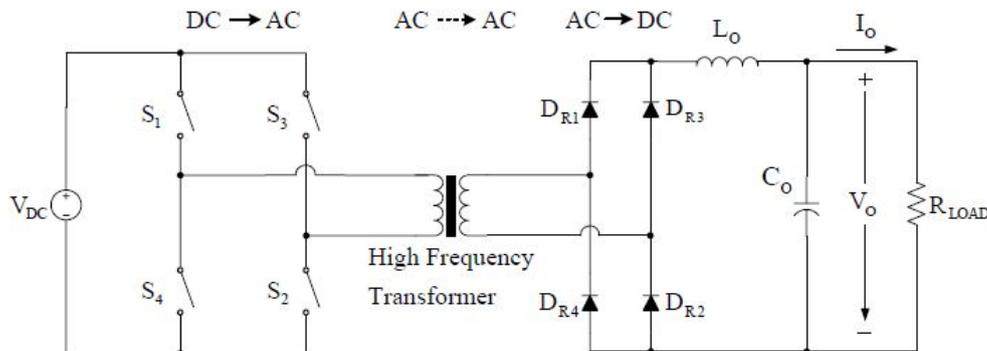
Figure 1.3: Basic scheme of the converter

The basic configuration of the full-bridge DC/DC converter, employs a full-bridge inverter, an high frequency transformer and an output rectifier. The switches are implemented by means of Mosfets, with a switching cycle able to output AC current at 100kHz. It should be underlined the fact that the DC/DC converter system consists of mainly two stages, DC/AC and AC/DC stages. Thus, the name DC/DC converter here is attributed to the system, rather than to the individual converter subsystems. A classical converter working cycle consists of periodic turn-on/turn-off actions that change the mosfet state,

used as switches for this project. With no additional controls and components added to the architecture, these actions are called of "hard-switching", meaning that mosfet *under tension* are forced to stop conducting, which in a lifetime brings *losses proportional to the switching frequency*. This issue becomes particularly debilitating for those systems working at high frequencies like this converter, which benefits from higher energy flow but suffers of high switching losses.

The solution to this problem lies on **soft-switching techniques**, that under some hypothesis discussed in the following allow a null power loss due to commutations.

Soft-switching techniques make use of *resonance* between parasitic components within the converter that, if properly timed, can allow a no-losses switch of the mosfet meant to change state. Thus, the use of additional components is suggested in case the parasitic ones present in the system are not sufficient for fulfilling the requirements of resonance and energy transfer, mathematically described in the following. These components are external capacitors for the switches (Figure 1.4) and an inductor in series with the transformer, called AC inductor and main subject of this thesis.
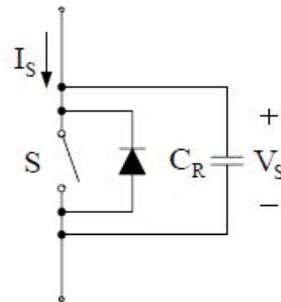
Figure 1.4: The elementary resonant switches for ZVS

The main purpose for these parts is to charge and discharge in a desired fashion so that the mosfet meant to commute does it only when its corresponding capacitor is completely discharged, so that no losses occur. Ideally:

$$\Delta V_{\text{mosfet}} = \Delta V_{\text{capacitor}} = 0$$
$$P = I * \Delta V = 0$$

The diode is present for both safety and practical reasons. Firstly for preventing undesired bias for the switch, secondly because the diode creates the switching window (called *dead time*, or *time delay* in which voltage across the switch is kept to zero, allowing the correct timing for the commutations.

As a matter of fact, while a component resonates, the voltage across it is zero once each half period, whereas with the introduction of a diode an alternative path for undesired currents during the negative voltage half cycle is established.

Actually, considerations about energy must be also taken into account. The inductor, which resonates with the capacitors, must have *enough energy* for charging and discharging them till the zero voltage condition is reached. If the energy condition is not fulfilled, the resonance will not be strong enough for ZVS.
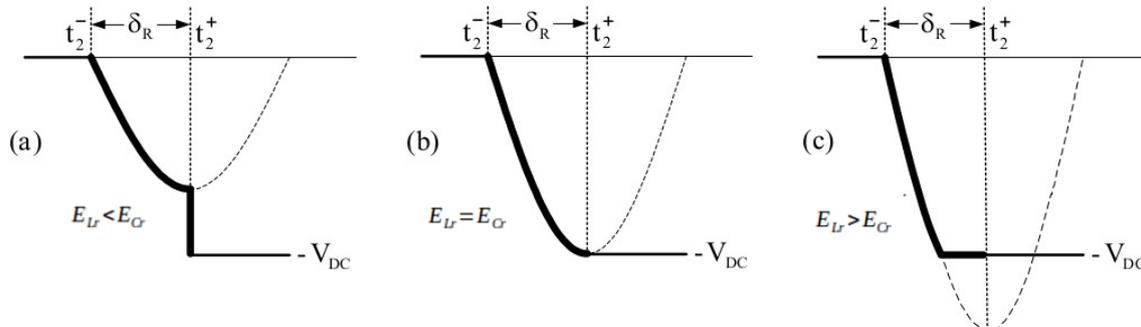
Figure 1.5: Three cases for energy in parasitic elements [δ=dead time]

Therefore, due to the energy expression for an inductor $E_{L_r} = \frac{1}{2}L_r I^2$, a condition on the load must be introduced so that the minimum current level for resonance is reached. Summarizing, the basic conditions for a successful ZVS are:

- Condition on *Dead time*, which is related with to the quarter of the resonance period:

$$t_{delay} > \frac{\pi}{2\omega_r}$$

where ω_r is computed by

$$\omega_r = \frac{1}{\sqrt{L_r C_r}}$$

being L_r and C_r the resonating components;

- Condition on *Energy in parasitic elements* (either intrinsic or added) which fixes boundaries on *load* and *inductances/capacitances* by the relation

$$E_{L_r} = \frac{1}{2}L_r I^2 > \frac{1}{2}C_r V_{IN}^2 = E_{C_r}$$

.

Being the second condition more related to the choice of components for the converter, it will be discussed in Chapter 3 with the inductor design.

Until now, only a lower bound has been defined for the t_{delay} but, actually, the control signal must respect both lower and upper limits. As a matter of fact, if the switch commutes while its relative diode is not conducting, the waveform in Figure 1.6 might occur.

In this case, the ZVS is not achieved, being the voltage across the switch different from zero.
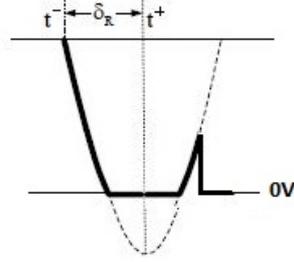
Figure 1.6: t_{delay} upper bound not respected

At this point, it should be clear that the coordination of the control signals is a difficult task. Now it is going to be described the model to be achieved by the controller, along with brief descriptions of the relations between each component.

1.2 Half of a period in Phase Shifted ZVS mode for a Full bridge converter

It has been described the importance of resonance for this SMPS (*Switching Mode Power Source*), but how to implement it during a whole cycle, maintaining the wanted inverter functionality of this converter?
The main difference between this implementation and a common Full Bridge SMPS is the phase shifted control of the switches.

Figure 1.7: The FB-PS-ZVS DC/DC converter circuit diagram.L_{Lk} is the L_r previously used

Figure 1.8: Transformer primary voltage, primary current, and secondary voltage waveforms of the FB-PS-ZVS DC/DC converter.

As a matter of fact, the full bridge is divided in a *leading lag* and a *lagging leg*, depending on the order of switching on and off. In this case, we consider that the gate PWM signals of T2 and T3 are delayed (phase-shifted) with respect to those of the switches T1 and T4, being the left leg the leading one and the right leg the lagging one. An immediate graphical explanation of phase-shifted control is reported in Figure 1.9.
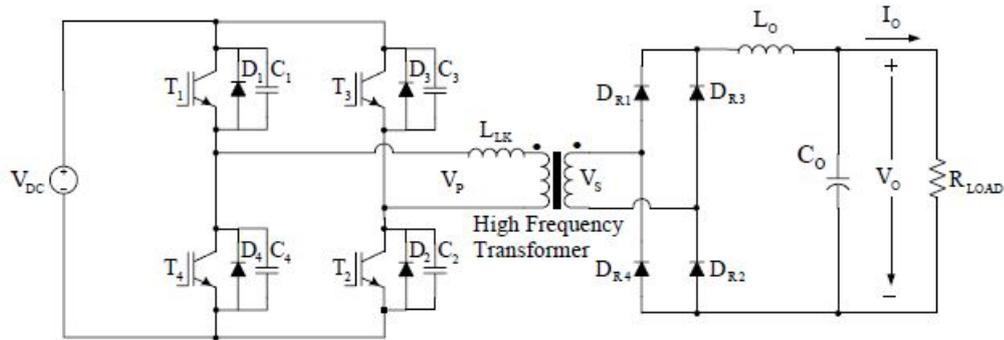This differentiation is necessary because, as it will be underlined in the following, the behavior of this converter is *asymmetrical*, meaning that the two legs have different impacts on the secondary voltage.

The ratio between the total duration of the voltage ($+V_{DC}$ and $-V_{DC}$) applied to the transformer primary winding in a switching period, and the switching period itself is symbolized as d_O and stated on the transformer primary voltage waveform. According to the time delay t_d and to the corresponding d_0, the output voltage of the DC/DC converter can be increased by decreasing the phase shift angle or vice versa.

As can be notices from Figure 1.9, the transistors are not always diagonally coupled as in a traditional Full Bridge. There are intervals in which T1 and T3 are conducting at the same time, the same as T4 and T2 in their intervals.

This horizontal coupling between two switches allows the interaction between same-leg switches, more precisely between their capacitors in parallel, letting the transistor that is going to be turned on discharge its own capacitor, resonating with L_r and therefore charging the other coupled capacitor.

However, this applies only for lagging leg, cause the leading one always commutes from
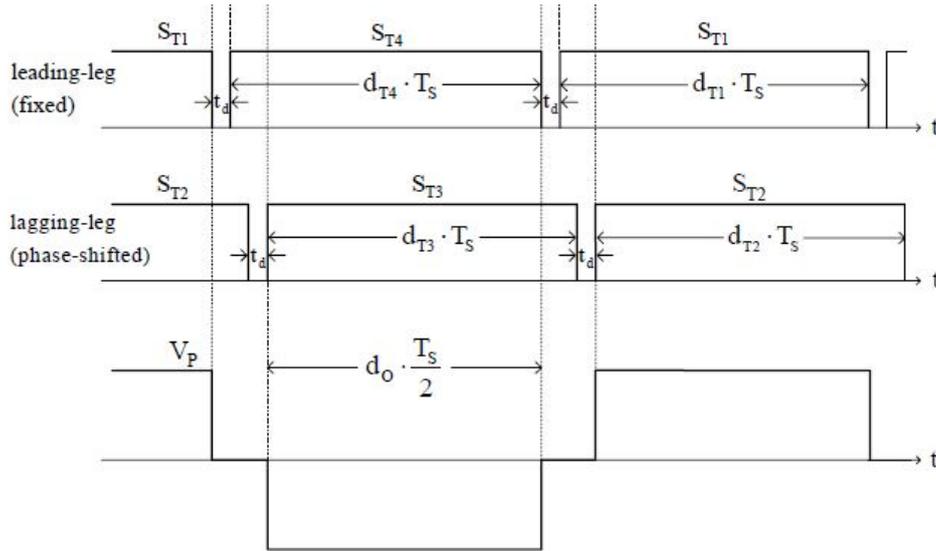
Figure 1.9: Switch gate PWM signals and the resulting transformer primary voltage.

diagonal-ON configuration.

This is not a problem, being the inductor fully charged for the leading commutation, ensuring ZVS even for the leading lag. Actually, the lagging lag comes to be the most cumbersome, mainly due to the de-energized L_r. It must be also taken into account that we do not consider the magnetizing inductor in this reasoning due to its high inductance, that at high frequencies makes it an almost opened circuit.

A brief description of each section of a period is going to be provided, referring to the the current-secondary voltage plot (Figure 1.8).
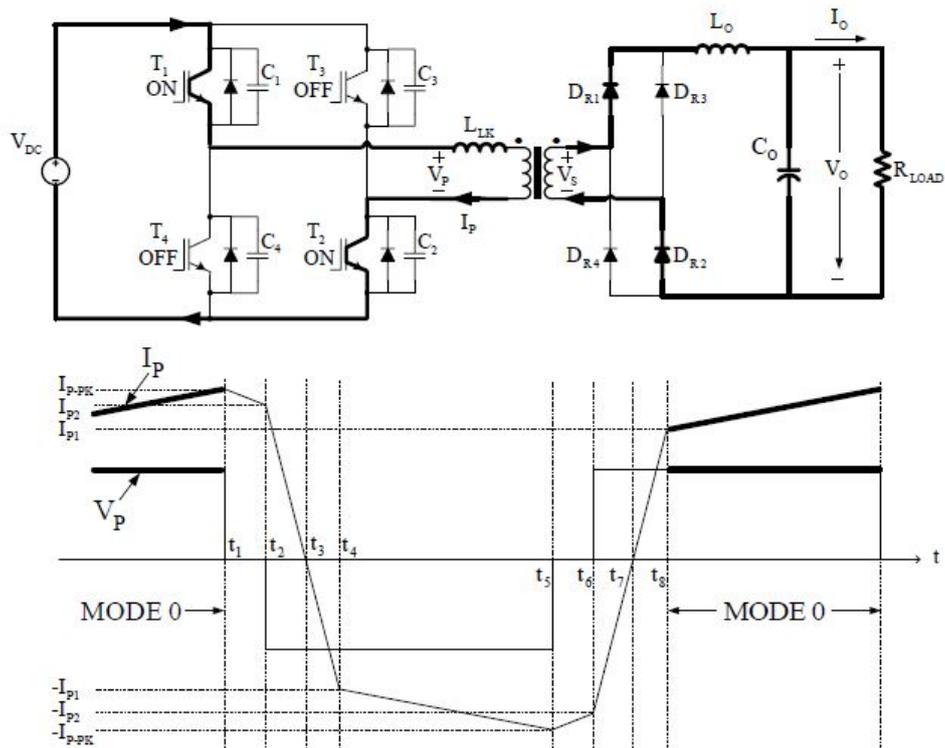
1.2.1 Mode0

Figure 1.10: The circuit diagram and primary voltage and primary current waveforms of the FB-PS-ZVS DC/DC converter in mode 0.

This Mode0 is characterized by T_1 and T_2 active, as represented in Figure 1.10: active power is transferred from the primary circuit to the secondary.

It must be underlined that capacitor C_1 has no charge, due to T_1 switched ON, whereas C_4 is under the whole V_{DC} voltage, neglecting minor voltage drops due to copper and mosfet, and therefore is charged.
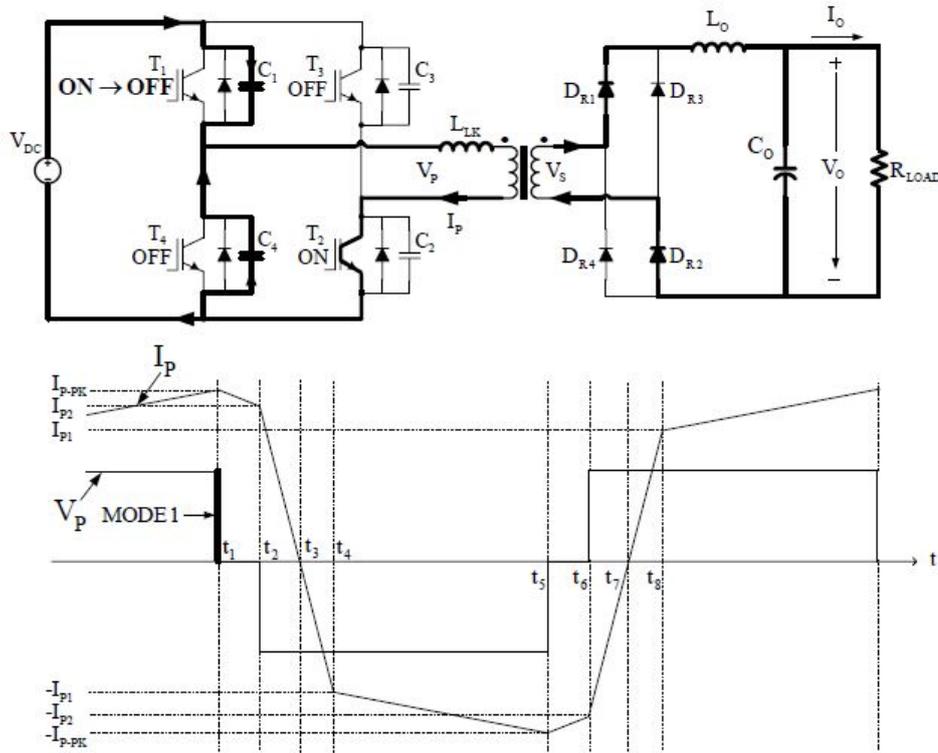
1.2.2 Mode1

Figure 1.11: The circuit diagram and primary voltage and primary current waveforms of the FB-PS-ZVS DC/DC converter in mode 1.

T_1 is switched off, but because of the inductances action, current continues to flow in the same direction, charging C1 while discharging C4. At the end of this mode, the voltage across C_1 clamps to V_{DC} and the voltage across C_4 decreases to zero. This mode1 lasts for a very small interval, just the time needed for ensuring the ZVS of T_4.

Moreover, due to the previous active power period Mode0, both leakage inductance and output filter have energy accumulated that can be provided for charging and discharging the two capacitors. This makes ZVS in Mode2 easier than the one in Mode3/Mode4, when the energy is limited (Figure 1.11).
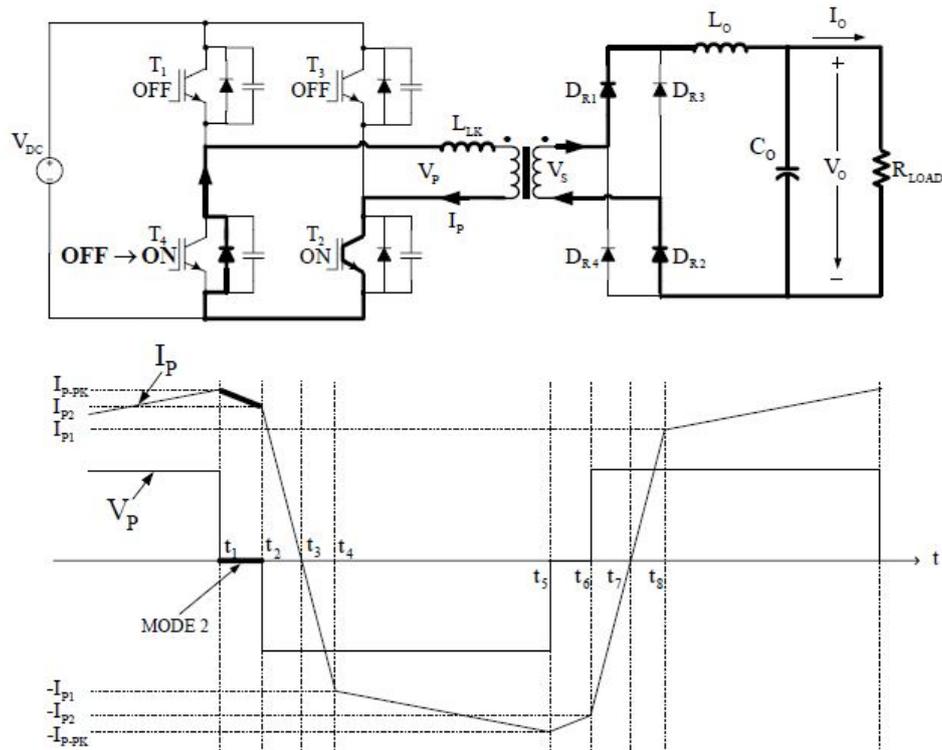
1.2.3   Mode2

Figure 1.12: The circuit diagram and primary voltage and primary current waveforms of the FB-PS-ZVS DC/DC converter in mode 2.

In Mode2 T_4 is switched on. This makes the voltage applied to the transformer equal to zero. Actually, T_4 does not belong to the primary current path, cause the inductor forces the current to flow in the same direction as Mode2: in spite of T_4, its corresponding diode is indeed conducting (Figure 1.12).
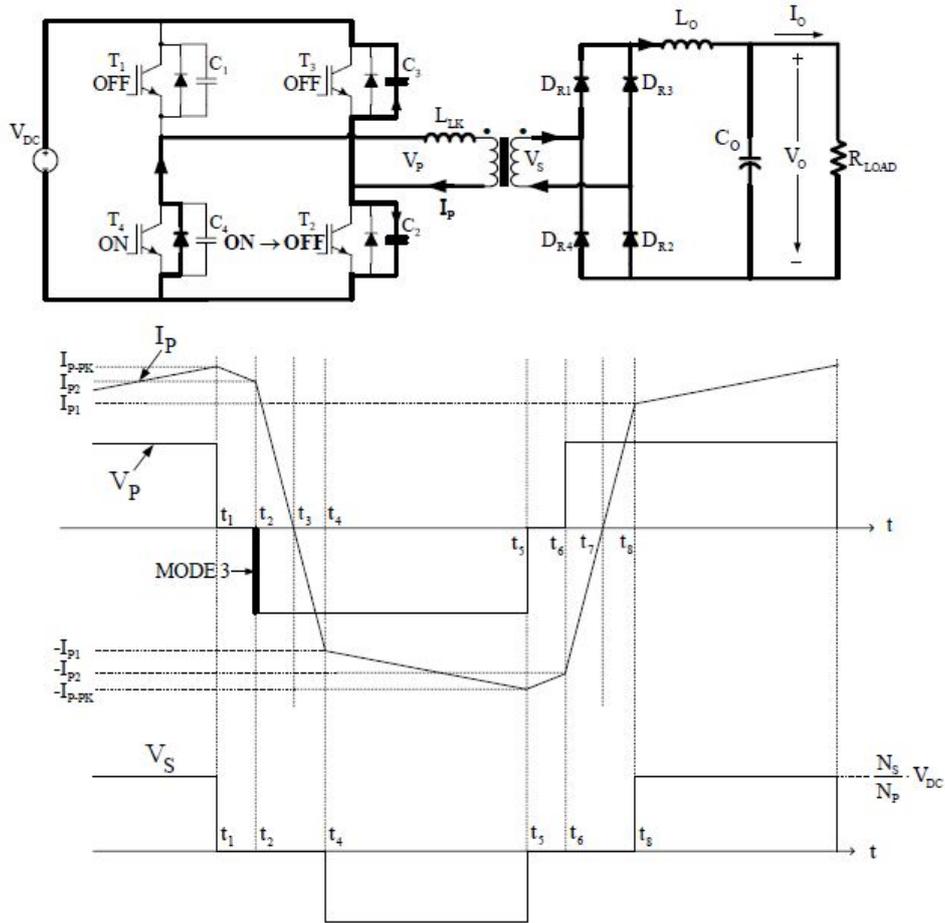
1.2.4   Mode3

Figure 1.13: The circuit diagram and primary voltage and primary current waveforms of the FB-PS-ZVS DC/DC converter in mode 3.

When T_2 is switched off, as occurred in Mode1, the two capacitors on the same leg interchange energy by means of the inductor. However, Mode3 does not follow an active power stage, which means that both inductor and output filter have only the energy left after the leading leg switch. This makes this mode the most critical among the others. Here mostly applies the reasoning of section 1.1 about resonance between components. It's worth to notice that each one of the four diodes in the output rectifier is conducting. This is due to the charging process of C_2. At a certain point, the voltage across C_2 is going to be greater that the voltage drop across the leakege inductance, which yields the activation of diodes D_{R3} and D_{R4}, as occurs when V_S is negative and, along with the other two active, clamps the secondary voltage at zero (Figure 1.13).
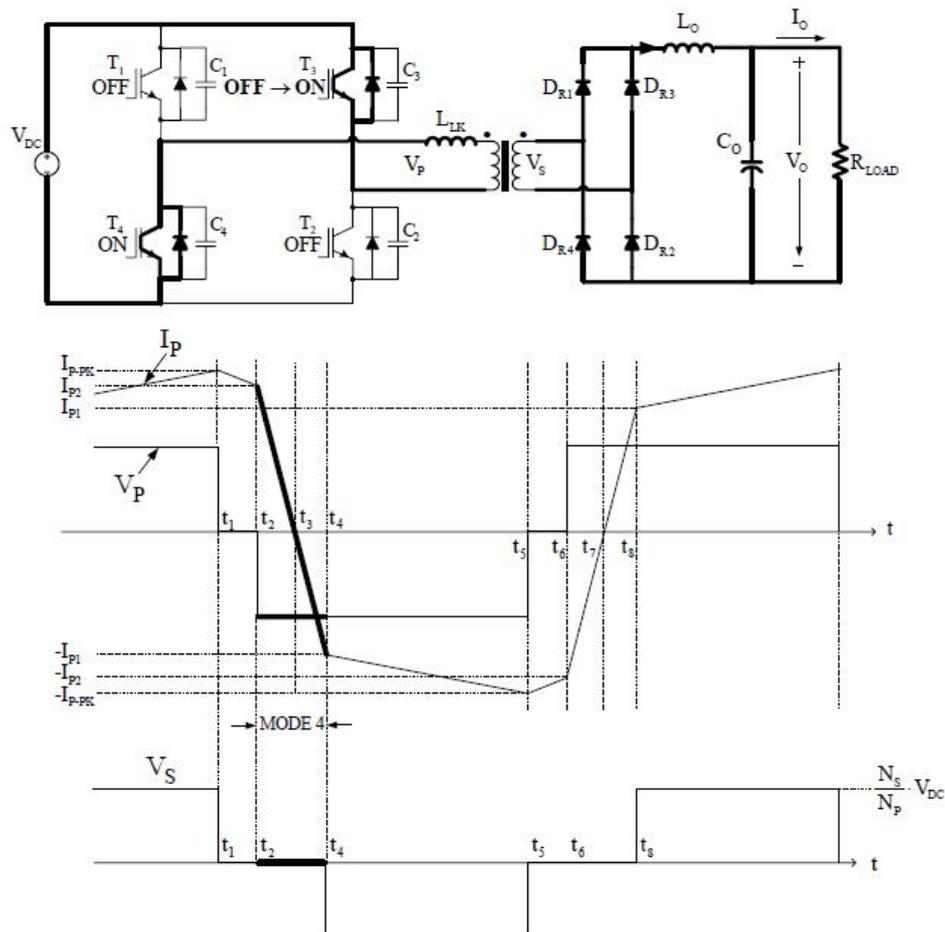
1.2.5 Mode4

Figure 1.14: The circuit diagram and primary voltage and primary current waveforms of the FB-PS-ZVS DC/DC converter in mode 4.

When C_3 is completely discharged, the ZVS for T_3 can be achieved. Then, once T_3 is switched on, its diode begins to conduct, due to the direction of flow. However, at t_3 the current reverses and the Mosfet T_3 itself can conduct.

In Mode4 V_S is still equal to zero cause each output diode conduct due to the reverse recovery. In fact, each diode needs some time to pass from conducting condition to open circuit, mainly because of the parasitic components present in each of them (Figure 1.14).
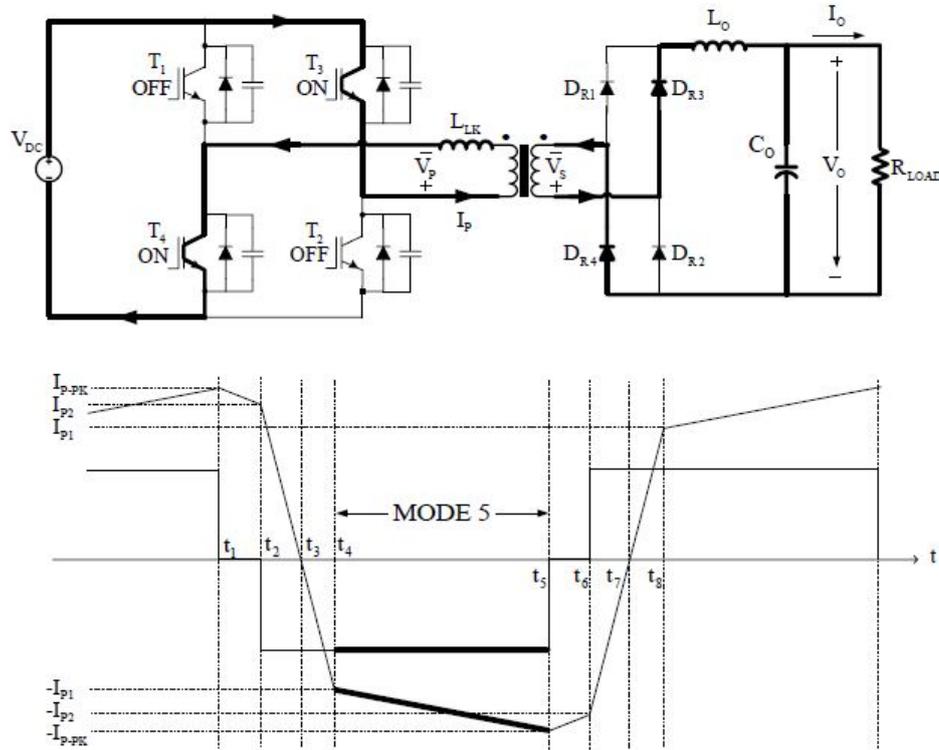
1.2.6 Mode5

Figure 1.15: The circuit diagram and primary voltage and primary current waveforms of the FB-PS-ZVS DC/DC converter in mode 5.

The last stage for this half cycle is Mode5, when diodes D_{R1} and D_{R2} stop conducting. That means a negative voltage is applied to the secondary, and active power flows from the input to the output (Figure 1.15).

Concluding this description of the half cycle for this converter in phase shifted ZVS, few particularities have to be specified:

- It's been analyzed the process for achieving the configuration T_3T_4 ON from configuration T_1T_2 ON. Although this covers only half-period, the remaining half is specular;

- The lagging leg switches T_2 and T_3 turn on with ZVS when the stored energy in the leakage inductance of the transformer is adequate to charge and discharge the capacitors C_2 and C_3. However, the leading leg switches T_1 and T_4 turn on under ZVS condition for lower load current values since the stored energy in the output filter inductor is utilized additionally in this switching transition;

Although this seems to be a satisfactory design for a converter, the goal of maximizing the efficiency needs additional attentions. In the following, few diodes will be added to

the architecture, and a description of their role will complete the chapter regarding the converter.

1.3 The clamping diodes

In order to ensure lossless transition, especially at light loads that provide small currents and therefor low energy level for switching, it is desirable to have a large commuting inductor.However, the inductive source impedance causes voltage overshoot during the decaying portion of the reverse current in the diodes. This voltage overshoot and ringing can generate excessive losses or unwanted EMI (Electro-Magnetic Interference).

A good method for avoiding this effect is to *clamp* the junction of the transformer and the commutating inductor to the supply rails with two diodes (D_5, D_6 in Figure 1.16).
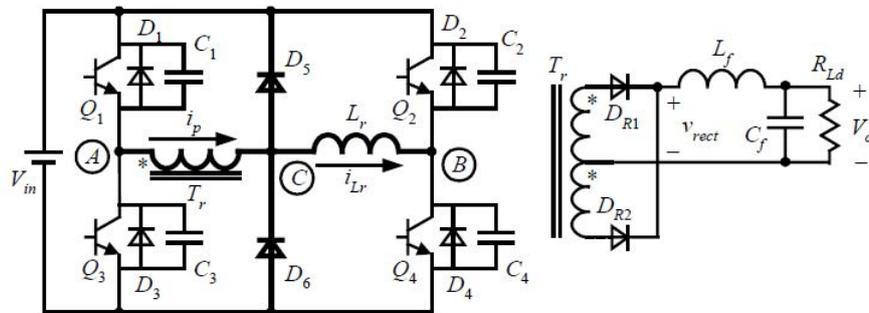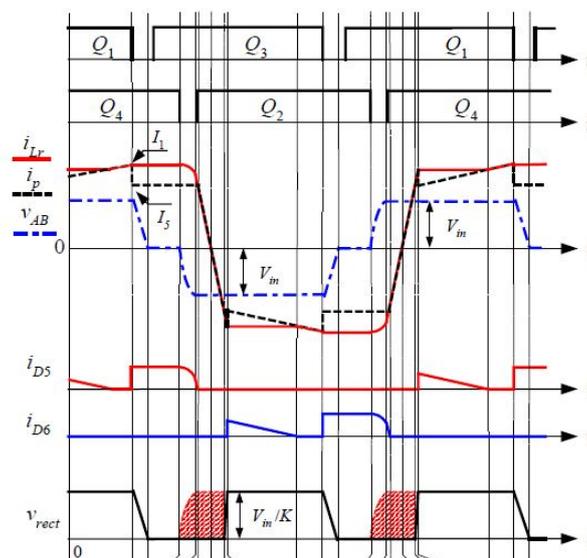

Figure 1.16: Main circuit with clamping diodes.

Figure 1.17: Key waveforms ZVS PWM full-bridge converter with clamping diodes

In Figure 1.17 the conducting intervalls for these diodes.

The next chapter will focus on some key aspect of the planar transformer present in the converter, especially regarding losses and efficiency.

Chapter 2

Iron and copper losses

The realization of the final AC inductor converter must take into account the non ideal effects present on the final components, being these the key points that once improved might determine the quality of the designed inductor with respect to others. These source of losses might be classified as **copper losses** , which affect the conducting wire, and **iron losses**, related to magnetic couplings between and within materials. These are unavoidable factors of any electric design process, although some techniques are adopted for limiting their impact on the system's performances.

2.1 Iron losses

Regarding iron losses, the two main kinds that have to be considered are **eddy current** losses and **hysteresis losses**. It might also be possible to include **flux leakages** as intrinsic losses mainly caused by geometrical properties of the system. In order to limit these phenomena, the designer needs to act against the net magnetic flux inside the core, maintaining that as low as possible during the whole AC cycle. As a matter of fact, both eddy currents (2.1.1) and hysteresis losses (2.1.2) are related to magnetic flux, as it is going to be discussed in the following sections.

2.1.1 Eddy current losses

In an inductor, alternating current passes through the coil, which produces alternating magnetizing flux in the core where the wire is wounded. However, according to the Faraday's law, a variation of flux in time determines a locally induced emf (*electromagnetic force*). Due to these emfs, there would be currents circulating locally, with no contribution in the active power at the output, called **eddy currents**. These circulating current will in point of fact dissipate heat causing a diminished efficiency.

$$\Delta i \rightarrow \Delta \phi \rightarrow e.m.f \rightarrow \text{local } i_{Ed} \rightarrow Ri_{Ed}^2 = \text{Losses}$$

2.1.2 Hysteresis losses

Given the hysteresis curve for the core material, we can associate a magnetic field H to an induction field B depending on the previous state of the ferromagnetic material. Furthermore, as stated by the Ampere's law, the magnetic field is related to current by

$$\oint B ds = i$$

and the energy consumed during one complete cycle of magnetism is

$$W = \int_0^{B_{MAX}} H \, dB = \text{Area of the H-B characteristic curve}$$

Therefore, the energy loss is indeed related to H and its behavior in time, and consequently to Δi (in our case, the whole AC current).
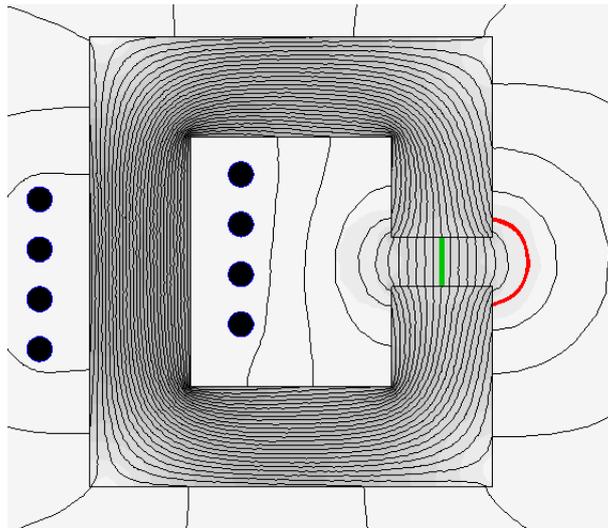
2.1.3 Flux leakages

Figure 2.1: Example of leakage in air gap

Electric components in relation with magnetic fluxes always experience some leakage phenomena, where by leakage it's meant something that *escapes* from the ideal path depicted for the circuit. This is mainly caused by ideal assumptions that, in reality, are not consistent, such as magnetic permeability of air and ferrite. This property, denoted with μ, describes the ability of a material to support the formation of a magnetic field within itself, and even if frequently approximated to zero compared to ferrite's one, even air has its own permeability.

This, expecially in cores with *non-distributed air gaps*, causes unwanted shapes of the flux, which consequently promotes the formation of disturbing current distributions along

its path as described in Chapter 3. For these reasons, the designed inductor will present distributed air gaps so to limit leakages.

Usual practice is the description of leakages by means of an inductance value, called *leakage inductance*, that normally depends on the geometry of the core and the windings.

In reality, as far as the design of an inductor is concerned, Eddy currents and Hysteresis losses come to be considered while choosing the component, making calculations based on data-sheets and observing B-H characteristics for limiting the flux. But, when the final arrangement needs to be designed, the most critical aspects to be faced are related to position and orientation in space of the conductive object, called **skin effect** and **proximity effect**. An introductory description of these two is necessary for further analysis.

2.2 Copper losses

This design process is particularly keen on the containment of copper losses, especially against those related to the current distribution inside the conductor. As a matter of fact, the main phenomena that affect conductors and cause losses in the wire are **Joule losses**, **skin effect** and **proximity effect**. More in particular, the last two are caused by the superposition of magnetic effects, causing inhomogeneous current distributions that worsen the Joule losses present in the system. A more accurate description of these three in the following.

2.2.1 Joule losses

Copper losses result from Joule heating and are physically expressed by the formula:

$$P_{\text{copper}} = R * I^2$$

where R is the resistance of the material, in turn expressed as

$$R = \rho \frac{\ell}{S}$$

being ρ the resistivity, ℓ the length of the conductor and S the active section of copper. Skin and proximity effect cause an increased resistance of the conductor by diminishing the active section, which indeed worsen the problem of losses and heat production.

In order to limit how copper losses affect the system, the designer is going to minimize the length of copper used for windings which reduces the resistance and consequently the dissipated power, as well as limit the presence of skin and proximity effects that indirectly worsen the Joule heating.
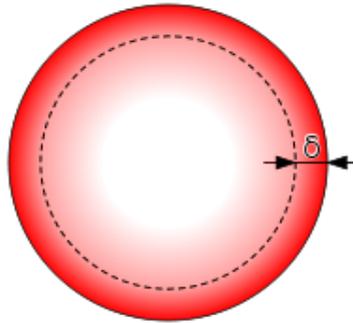
2.2.2 Skin effect

Figure 2.2: Distribution of current flow in a cylindrical conductor, shown in cross section. For alternating current, most (63%) of the electric current flows between the surface and the skin depth, ρ, which depends on the frequency of the current and the electrical and magnetic properties of the conductor.

Considering a wire in which AC current flows, as it has previously been discussed (2.1.1), eddy currents appear as consequence of the varying flux. The so-called "skin effect" is the result of all eddy currents present inside the single wire.

The overall phenomenon is that in the inner part of the wire, the nominal current is summed with eddy currents flowing in its opposite direction, whereas near the surface both eddy currents and nominal ones have the same direction. The graphic representation of this in Figure 2.4.
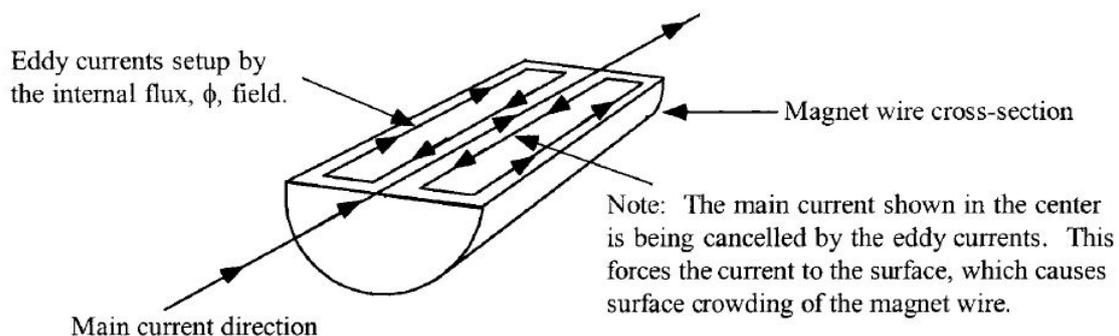

Figure 2.3: Skin effect graphically

The main problem related to the skin effect is the *non-use* of a big percentage of copper for conducting current.

This fact yields an increase of the resistance, with the consequent increased loss density, as explained in the beginning of the chapter.

Therefore, the less conducting surface, the more losses.

2.2.3 How to limit skin effect

The most widespread way to mitigate skin effect in conductors is the use of **litz wire**.

The term "litz wire" is extracted from the German word, meaning "woven wire". Litz wire is generally defined as a wire constructed of individually film insulated wires, braided together in a uniform pattern of twists and length of lay. This multistrand configuration minimizes the power losses, otherwise encountered, in a solid conductor, due to the skin effect. Other methods are known in electrotechnology, such as tubes hollow inside for high current applications, but have no use in this project.

Figure 2.4: Litz wire examples

Litz wire shows its usefulness even against proximity effect, described in the following.
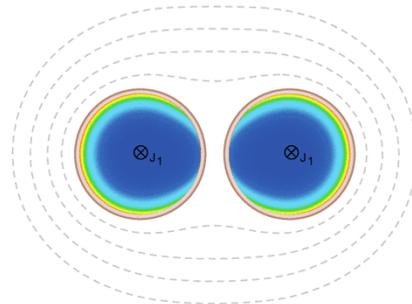
2.3 Proximity effect

Figure 2.5: Proximity effect on conducting wires

Proximity effect is caused by eddy currents induced in a wire due to the alternating magnetic field of **other** conductors in the vicinity. In fact, unlike skin effect, proximity effect is the result of a varying magnetic flux produces by *nearby* conductors under AC current. The eddy currents cause a distortion of the current density. This distortion is the result of magnetic flux lines that generate eddy currents in the magnet wire, therefore enhancing the main current on one side and subtracting from the main current on the other, as shown in Figure 2.6, producing an asymmetrical distribution on the single conductor.
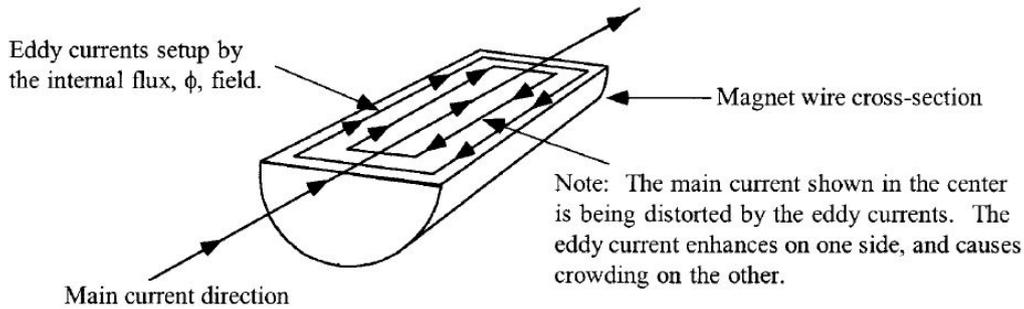
Figure 2.6: Proximity effect graphically

Proximity effect comes to be particularly problematic, for example, for multilayer transformer, where each layer has an influence on the others in terms of current distribution. The agent by which current's asymmetries appear is the magnetomotive force (mmf), or more accurately, the summation of every mmf present at each layer. An example of mmf distribution in Figure 2.7, where the central layers are subjected to mmf from all the other layers and therefore showing the highest density (For further details about the transformer design, [1]).
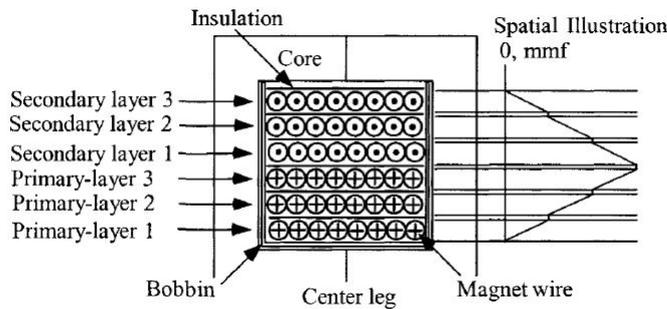
Figure 2.7: A Transformer, Showing the Magneto-Motive Force, mmf

2.3.1 How to limit proximity effect?

The main way for the mitigation of proximity effect lies on the use of special insulation techniques for cables. One approach could proceed in insulating as best as possible each wire, another could propose some sort of Electro-Magnetic shields for avoiding coupling for the specific application, even by means of foils. In the following, few graphical examples.

(a) Triple cable

(b) Triple litz
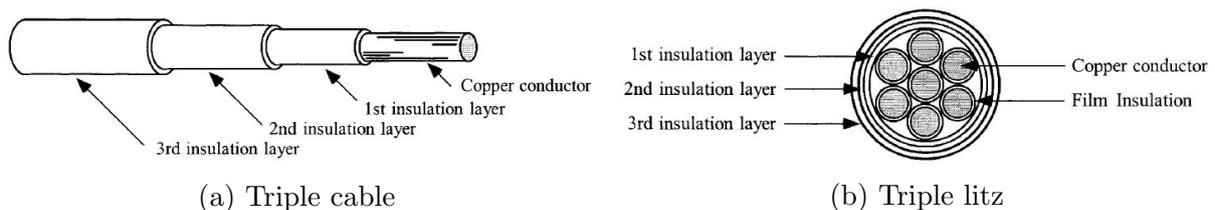
In the next chapter the design process of the inductor is going to be described in detail.

Chapter 3

The planar inductor

3.1 Comparison between planar and toroidal inductor

Although the final choice of the inductor has not been made yet, the design proposed in this thesis aims to substitute the planar inductor already installed on the converter with a more performing toroidal one.

The electrical characteristics for this component have to be:

- $I = 17$A RMS, peak-to-peak $= 42$A;

- Frequency $f = 100$kHz;

- Power $P = 1400$W;

- Minimum inductance $L = 8$µF. This value has been calculated so to be able to reach ZVS in the full bridge, as discussed in 1.1.
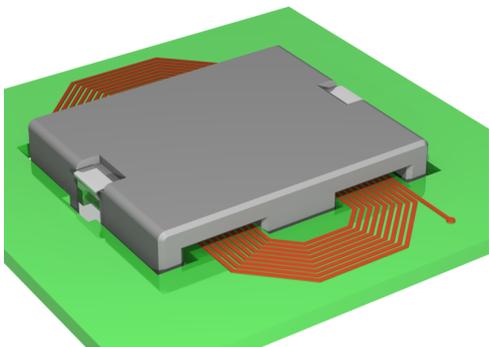
(a) planar inductor with printed conductor
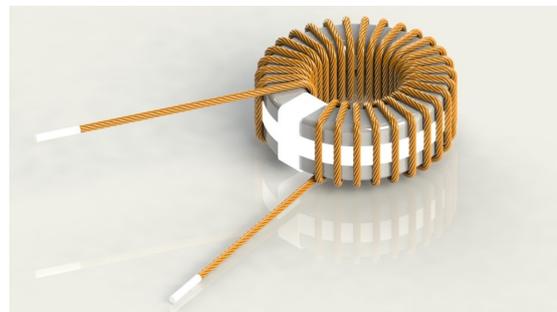
(b) toroidal inductor with litz wire

Figure 3.1: The two kind of inductors considered for the analysis

The first solution, in figure 3.1a, is a planar transformer realized by windings printed on multi-layers PCB with thickness around 200µm. The ferrite is an E-shape core, with non-distributed air gaps.

The second one, in figure 3.1b, is a more common toroidal inductor with ferrite core with distributed air gaps and litz windings.

As discussed in [2], the main advantage of a planar inductor are:

1. Presence of big board surfaces as well as natural passages for air flow, that would allow more efficient heat dissipation with respect to normal copper coils, one of the main concern for an high frequency transformer;

2. Cost-effectiveness, due to the relatively cheap PCB boards available on the market;

3. Easy integration in the final product with the other ferrites for the transformer and the DC-inductor;

4. Good reproducibility, making it good for large scale productions;

5. Unbounded to a specialized firm, being its single parts largely sold worldwide.

For these reasons, the first candidate as AC inductor for the charger was a planar solution. However, its performances under the nominal working conditions were not completely satisfactory, showing losses of 18W , heavy presence of skin and proximity effect, huge amount of leaking flux under magneto-static Femm simulations.

On the contrary, due to the geometrical characteristics of a wound toroidal inductor, the expected properties of this object before any simulation are:

1. Decreased leakages, due to the circular geometry of the product which follows the natural flux lines path, as well as distributed air gaps and natural "magnetic wall" formed by dense turns, which prevents flux from escaping;

2. Less iron losses by the use of litz wire;

3. More uniform distribution of current, leading to less specific copper losses. However, depending on the necessary number of turns, the total losses derived from copper might be larger than in pcb. On the other hand the direct exposure of wires to air could let the inductor benefit of smaller increase in temperature.

Each of these properties is going to be tested by means of simulations and theoretical analysis.

Next, the planar solution is going to be described.

3.2 Planar Inductor simulated

This implementation reflects the one used for the transformer, where multiple layers were stacked so to form the primary and secondary circuits, with E-shaped ferrite core forming non-distributed air gaps.
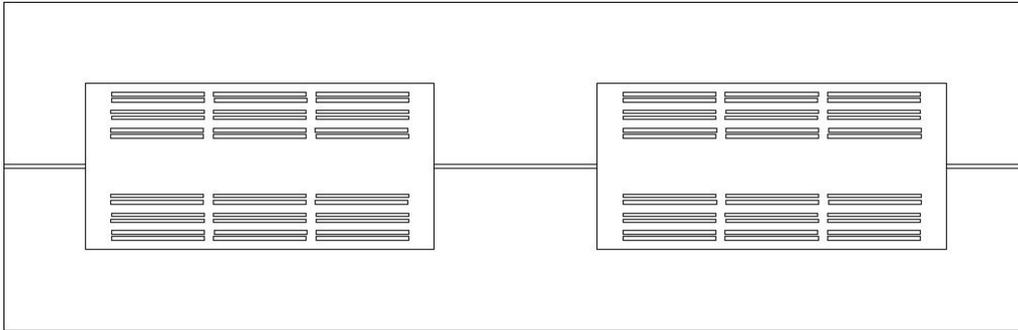

Figure 3.2: Section of the whole inductor, where layers have been represented just by the corresponding copper

For the sake of clarity, in the majority of the cases only half inductor will be shown, being the other half its symmetrical.

As analyzed in the first chapter (1), this planar inductor lies upon PCB layers with printed winding. In the following, copper windings will be denoted by rectangles with appropriate width and length, respecting the real dimensions of the vertical section of the board.

The analyzed configuration consists of 3 turns around the central ferrite column, with 12 coils in parallel, 6 in the upper part and 6 at the bottom. The core itself is composed of 2 E-shaped ferrite, where the separation is underlined by the air gaps of the structure. In order to save funds, both boards come from a previous design of the transformer, which consisted of a primary divided in boards with 3 turns each as in the case of the planar inductor.

Concerning the ferrite, the Ferroxcube 3C94 has been chosen instead of the older 3C90, mainly due to the worse performances of the latter in terms of losses around 100°C given a common value for the AC Flux (50 mT), as depicted in Figure 3.3.

The main aspect to be considered is the heat development under the stressful working conditions imposed by the converter. Therefore, electromagnetic simulations are needed for an estimation of the overall performances.

In particular, the key aspects to be investigated are:

- Total losses, useful for determining the increase in temperature and evaluate the efficiency;

- Flux distribution, which has to comply with the desired behavior of the system, also in terms of leakages;
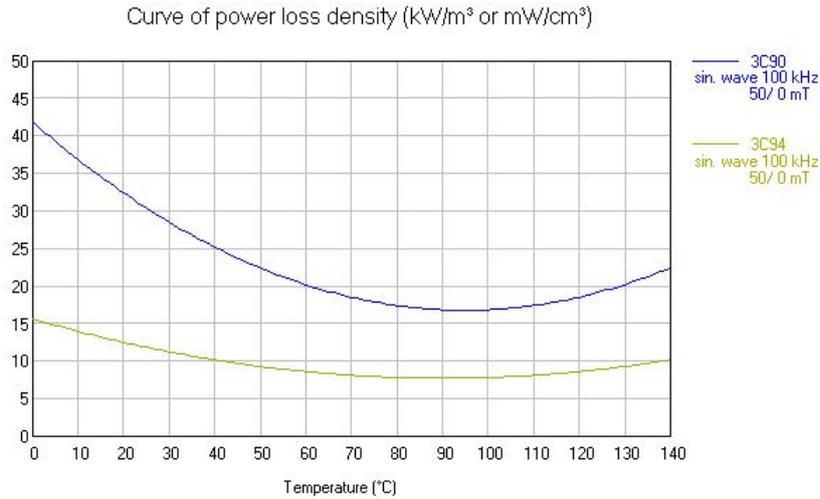
Figure 3.3: Ferrite characteristics using Ferroxcube Design Tool[losses over temperature]

- Total current distribution, particularly useful for evaluating the presence of skin and proximity effect in the considered configuration.

A first geometrical model comprises currents, materials and shapes of the components, making use of the software Femm for magnetic simulations.
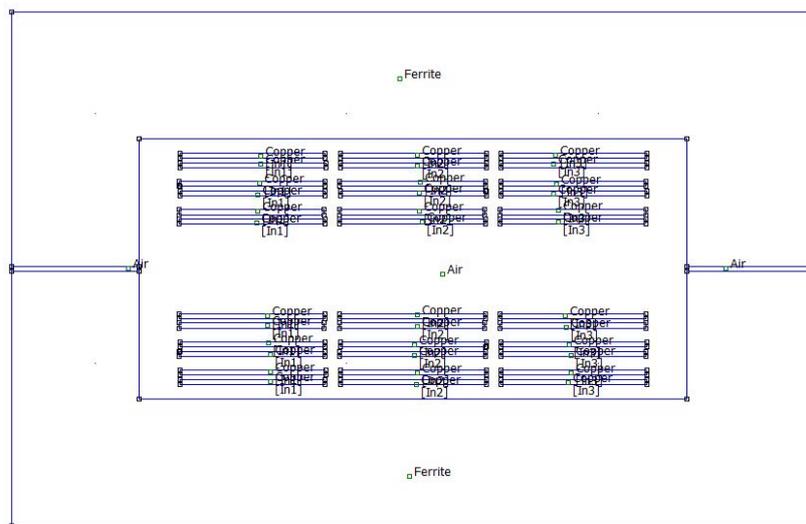
Figure 3.4: Modeling of the inductor in Femm

It is identical to half of the spoiled Figure 3.2, with the electrical and material characteristics in addition. It has to be pointed out that the simulation makes use of a 2-D model of the inductor with additional depth specification: this do not account for the complex geometry of wire curves in the third dimension, but it is sufficient for studying the effectiveness of a configuration and for making comparisons between models.

Now that the key aspects have been modeled, the simulation can take place. In particular, it's going to be shown the behavior of the current inside copper and the flux

lines distribution, listing the worth results.

- **Flux density**. As it was expected, the magnetic flux is almost all bounded inside
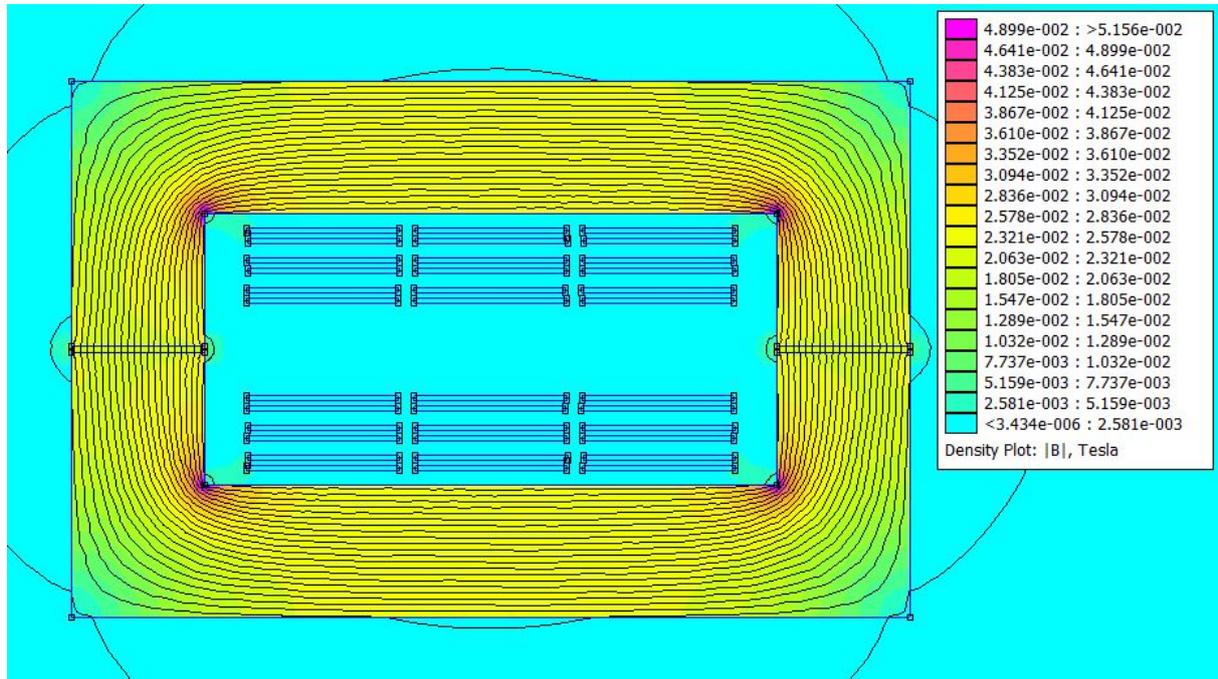
Figure 3.5: Flux Density

the ferrite core. However, once the number of flux lines showed in the simulation is increased, a not satisfactory presence of leakage flux is well noticeable (Figure 3.6). This is proof of the limits that a concentrated air gap brings to the system. In addition, the closer to the copper, the higher the flux density in the simulation
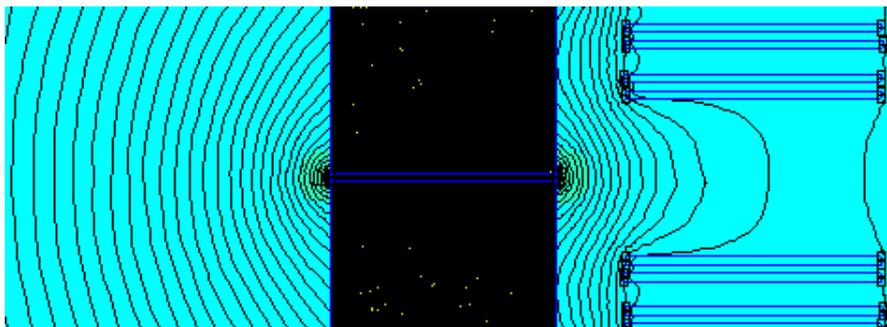
Figure 3.6: Flux Density, particular with more flux lines shown

of Figure 3.5. As a matter of fact, the copper conducts current with the same direction, and given the Ampere's law

$$\oint B ds = i$$

the length of the path is inversely proportional to the strength of the magnetic field. Therefore, the closer is the chosen path to the current source, the stronger and

denser the field will be.

Moreover, the presence of spikes yields to an accumulation of the flux, which determines the red color in the simulation.

- **Field Intensity**
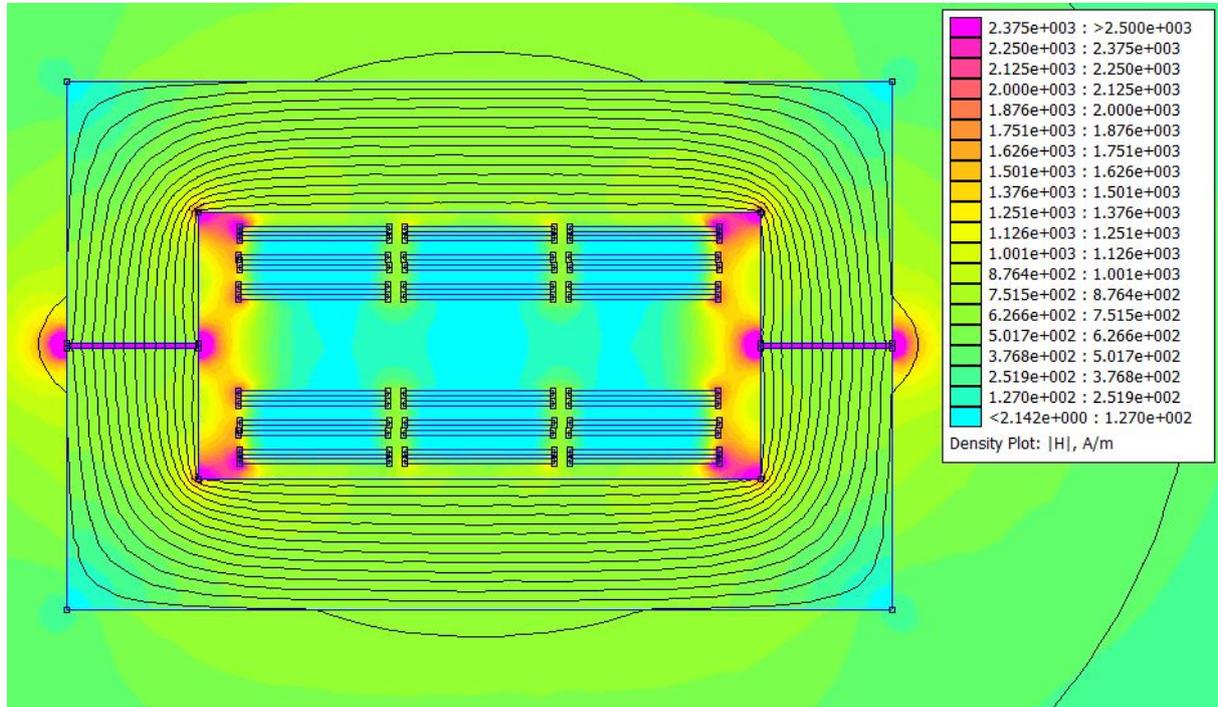
Figure 3.7: Flux Intensity

The figure presents high intensities where flux lines exit the conventional path inside the ferrite. When this happens, the permeability of the material drops (from ferrite to air) and according to Biot-Savart law, and relating magnetic flux and magnetic induction

$$\mathbf{B} = \frac{\mu_0}{4\pi} \int_\gamma \frac{I d\ell \times \hat{\mathbf{r}}}{r^2}$$

$$\mathbf{B} = \mu_r \mu_0 \mathbf{H}$$

the obtained relation is

$$\mathbf{H} = \frac{1}{4\pi \mu_r} \int_\gamma \frac{I d\ell \times \hat{\mathbf{r}}}{r^2}$$

Where the relation between field intensity and permeability is inversely proportional. Therefore, the field in air (low μ) will end up being more intense then the one in the ferrite (high μ).

- **Current Density** Probably the most important analysis, mainly due to the fact that copper usage is one of the key elements for preventing big losses in the inductor. What the designer would like to achieve is a good distribution along the whole

section of copper. This, given the already cited expression

$$R = \rho \frac{l}{s}$$

$$\rho = \text{resistivity}$$

$$l = \text{lenght}$$

$$s = \text{conducting section}$$

would yield a bigger section in which current flows, so diminished resistance of the circuit, lower losses and less stress for the material. An example of this behavior in Figure 3.8, which is the same half-planar inductor, but used at a frequency $f = 50\text{Hz}$. As immediately noticeable from the colors in the figure, the current
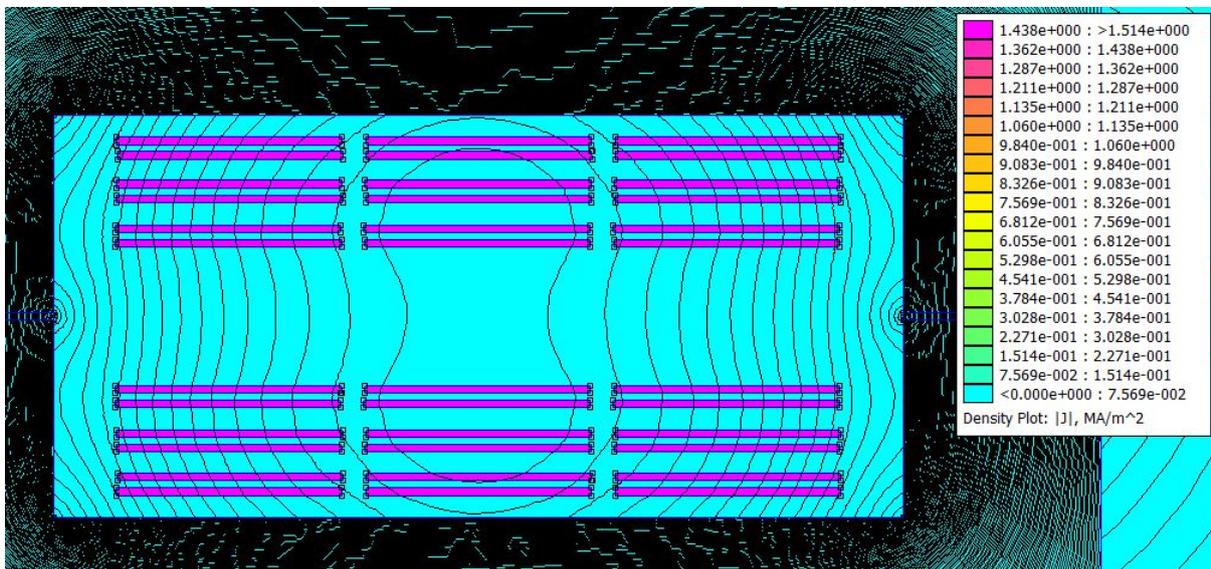
Figure 3.8: Current Density at 50 Hz

density distribution is *homogeneous* is each copper section. Conversely, as soon as the frequency increases, the AC effects become stronger and more evident. In the Figure 3.9 skin and proximity effect lead current to accumulate along the edges of the conductors.

Moreover, one of the main issue is the presence of back emf where the flux leaks from the core. In fact, it can be noticed that the field lines are not all regular: due to fray and air gaps, these lines tend to choose inner and short paths, vertically crossing the conductors. The developed back-emf rejects these fluxes, pinching the flux lines as in the figure

What might immediately be concluded from these results is that high frequency and high peaks of currents cause a huge amount of problems. However, pros could justify cons by an optimized design, so to enhance the efficiency of the system. The planar topology
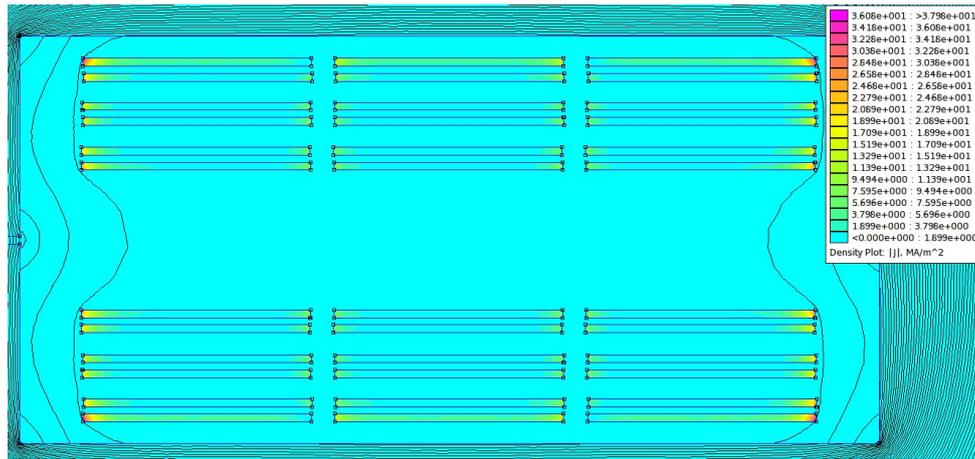
Figure 3.9: Current Density
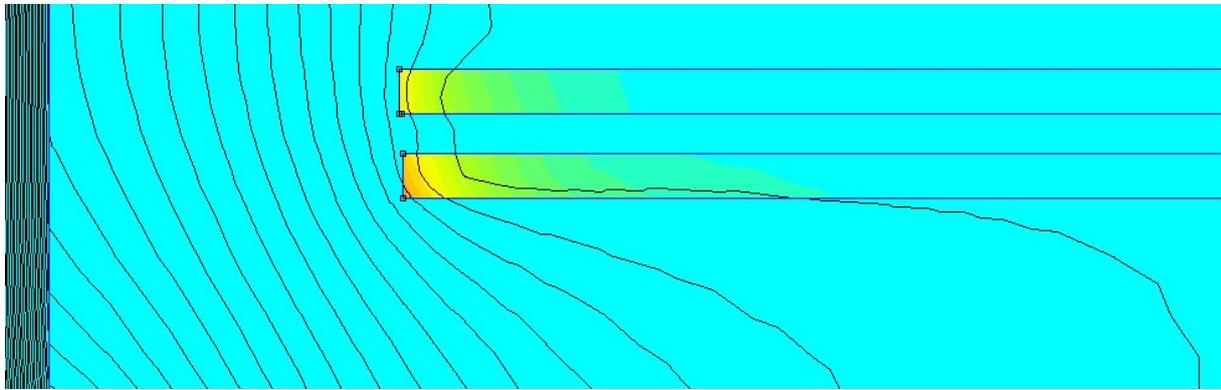
Figure 3.10: Flux lines deviation

itself of this inductor lead to risen losses, but on the other hand to large dissipation areas: as always, a trade-off that might be worth.

Numerically speaking, a theoretical way for judging the performances of the component under test is by measuring the losses directly from the simulation environment. In this case, selecting every copper portion in Femm, the software is able to calculate the total losses, that for this planar inductor are:

$$P_{\text{Losses}} = 2 * 0.89 = 1.8\text{W}$$

where the double has been considered for accounting the fact that the simulation displays only half of the symmetric inductor.

Beside leakages, another big issue is the presence of unused portions of copper (cyan color inside rectangles), caused by skin and proximity effect, both derived from eddy currents inside conductors. This practically means that even if the inductor is provided with a certain volume of copper, at 100kHz it is only able to use a small percentage of it, affecting the cost-effectiveness of this solution.

Based on the previous reasoning, a new approach to the problem in the next section.

3.2.1 "Chamfered" planar inductor

Figure 3.9 and Figure 3.10 underline the fact that, given an air gap from which magnetic flux leaks, whenever it crosses a conductor eddy currents and back e.m.f. are generated so to counteract against this flux. This is particularly true when the conductor is placed in an opposed fashion with respect to the flux lines, with the consequence of opposed emfs that "push" away the flux in non continuous distributions.

One of the proposed solutions for limiting this effects and consequently the losses is to shape the conductor following the ideal flux lines from the air gap, so to limit the $\Delta\phi$ which causes undesired currents.

The resulting topology has been realized "cutting" in Autocad the parts of conductor belonging to circles whose centers are pinned to the main source of leakage flux, in this case the sharp corners and the two air gaps of this half planar inductor. The body of the inductor in the drawing software has been sketched as in figure 3.11.
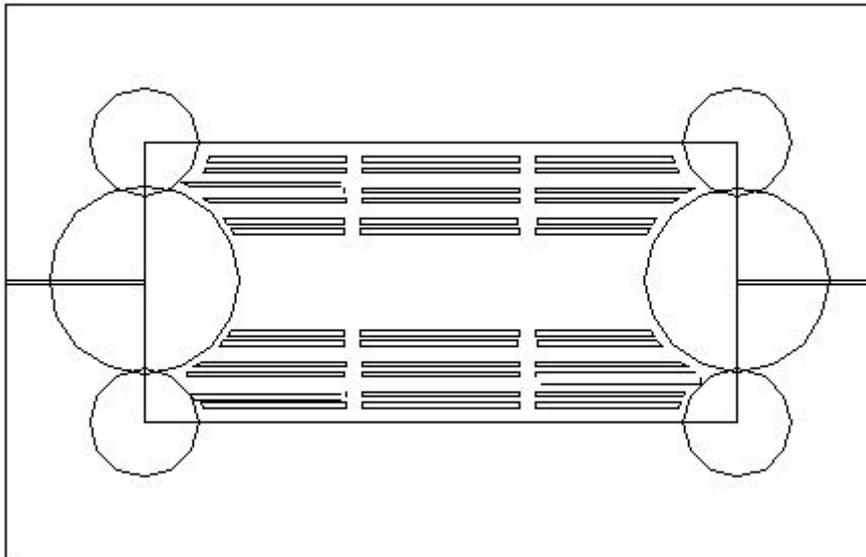
Figure 3.11: Way of drawing the chamfered copper tracks

and the implementation in Femm as in figure

Now a brief analysis of the results obtained by the new topology is held.

The plotted quantity that is expected to be the most different one with respect to the previous non-chamfered model is indeed the current density, for which we introduced these smooth profiles. What the designer would like to see in the simulation is a well distributed current, indeed unlike to happen, or at least lower current densities at the edge of the conductors. The simulation in Figure 3.13

The general view is unfortunately unsatisfactory. Looking at the legend, the peak of current density has risen with respect to the previous one in Figure 3.9, which could mean either increased losses due to eddy currents or less more unused copper, or even both. In each scenario, higher densities brings worse performances.
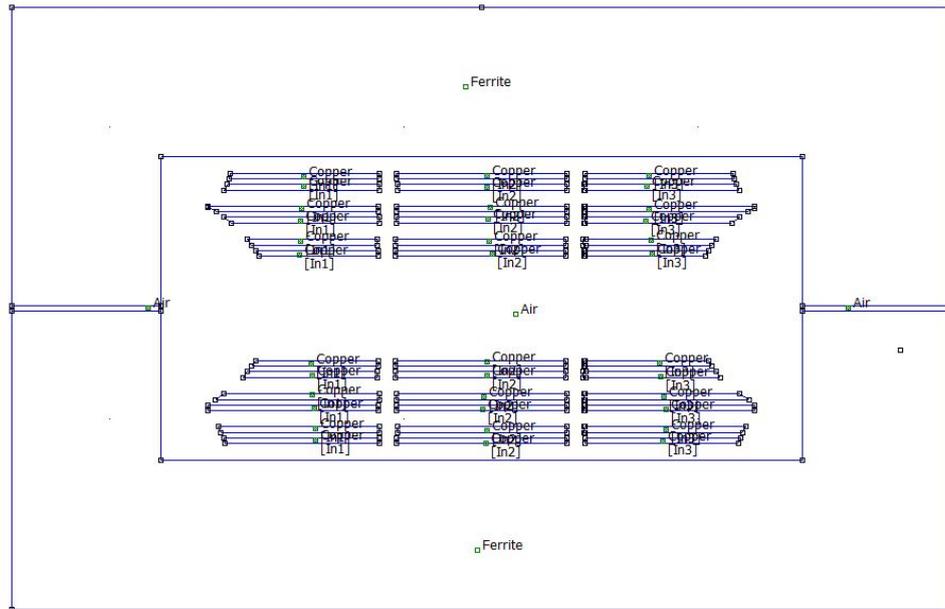
Figure 3.12: Implementation in Femm
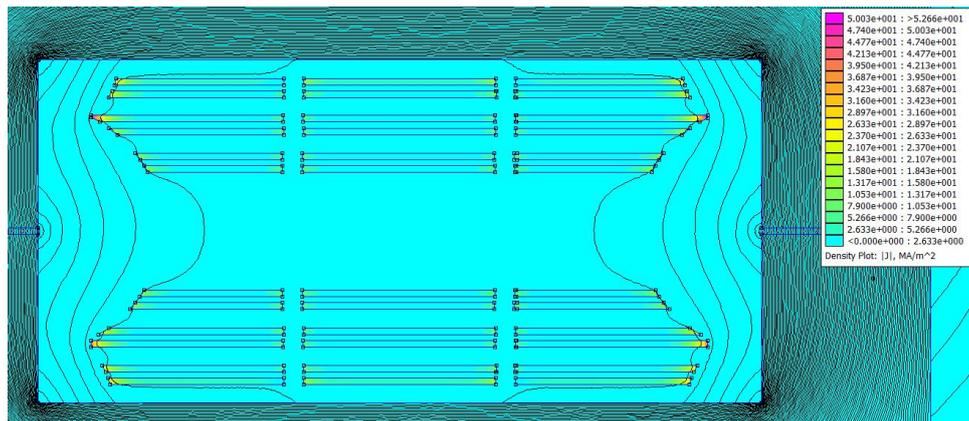
Figure 3.13: Section of the inductor

From a zoom, the worsen distribution of current might be confirmed by means of the color-code.

Even if the shape of the flux lines is indeed improved, the presence of sharpened portion of copper brings unwanted effects on the system.

As a matter of fact, selecting all the copper portions in the simulation and comparing the total losses reported by the software, the results are

$$P_{\text{Losses NO CHAMFER}} = 1.8\text{W} < P_{\text{Losses WITH CHAMFER}} = 2 * 0.99 = 2\text{W}$$

which means that no improvement seems to be achieved from this solution.

It might be worth to compare the two simulation with the same scale of greys, so to appreciate graphically the difference in distribution.(Figure 3.15)

In both figures, the upper bound of the scale has been fixed to $35\frac{MA}{m^2}$ and as we
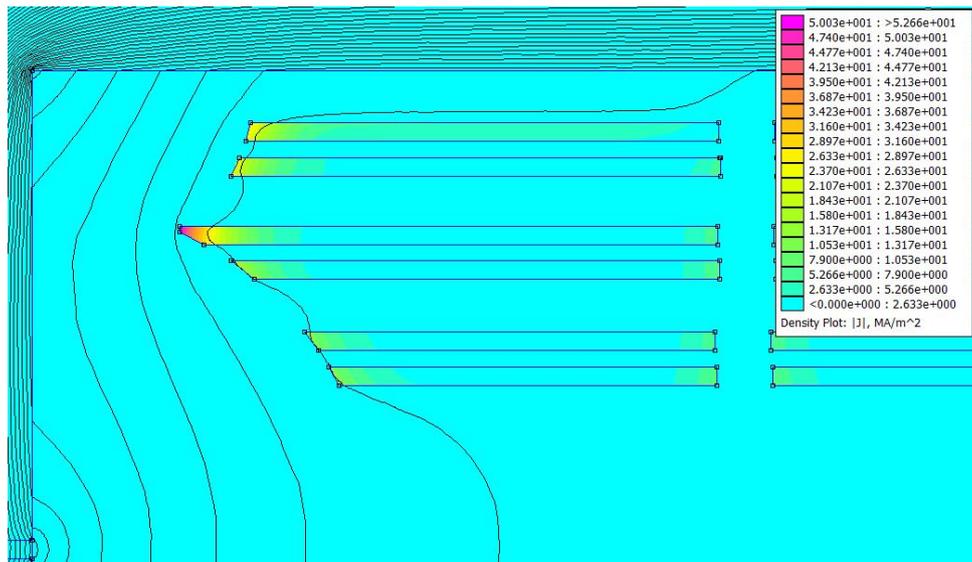
Figure 3.14: Zoomed portion for current distribution
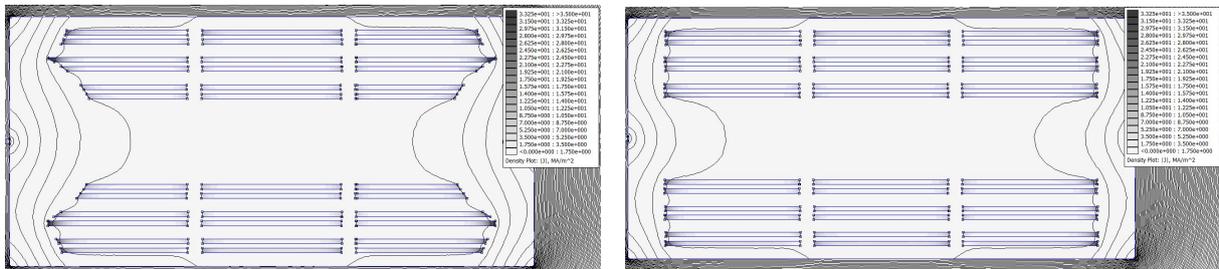
Figure 3.15: Comparison between the two solutions

previously underlined the new configuration does not improve the model.

Even with other shapes for the copper, the current distribution is still unsatisfactory.

The conclusion of these simulation is that the planar topology for this inductor does not fit with the requirements of the design, or it might be said that there could be better configurations to be chosen. The key problems are due to the arrangement of the windings, which exposes the inductor to an heavy presence of skin and proximity effect and, in parallel, the resulting leakage flux from the air gaps between ferrite cores.

In the following, the toroidal implementation will try to enhance the overall efficiency of the component.

Chapter 4

The toroidal inductor

Despite the good reasons for choosing a planar inductor that have been previously observed, the toroidal configuration might lead to better results for the charger, whose target is mainly high efficiencies with respect to usual high frequency components.

The two main issues met with the planar configuration were the isolated air gaps with the consequent leakage flux, and the heavy presence of skin and proximity effect. Both of these might be improved with the toroidal inductor, where the reasons are:

- *the presence of distributed air gaps*: this is a characteristic of the core, where the reluctance of the component is not related to a single air gap, but rather to an "equivalent series of air gaps" obtained by adding special plastic materials to the mix for the core

- *the arrangement of windings:* although the surface for dissipating heat is smaller then the planar configuration, the toroidal typology allows us to place the needed turns along the torus so that, under the proper number of turns, the copper itself limits leakage flux. More specifically, the more turns, the more bounded flux is obtained.

The first step to begin this design is the choice of technology to employ: in this case, considering the need of distributed air gaps, the *powder core* solution seemed the best one in terms of quality/price ratio.

Powder cores are distributed air gap cores that possess many useful characteristics, such as high resistivity, low hysteresis and eddy current losses, excellent inductance stability under both DC and AC conditions. Moreover, even if it is not of our interest during the design of this particular project, powder's DC Bias curve does not have the traditional saturation point that a ferrite core does, rather as the magnetic flux increases the permeability slowly rolls off in a predictable fashion.

The final product will look like the Figure 4.2, where additional insulators envelope the magnetic core, and the used of litz wire will need to mitigate unwanted inhomogeneous current distributions.
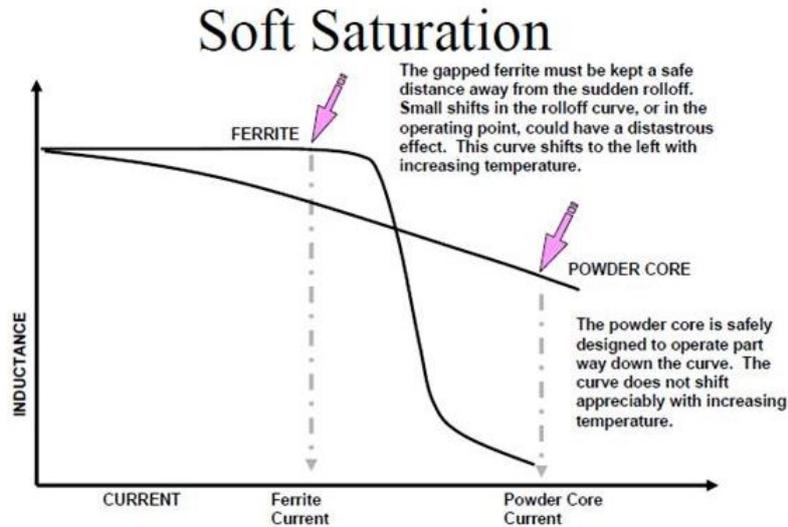
Figure 4.1: Comparison between ferrite and powder cores

Among the suppliers, the one considered in this project are **Magnetics** and **Micrometals**.

4.1 Algorithm for computing the parameters of the inductor

It's common practice for suppliers to provide specific software for the design of components that, given the specifications, enlist a series of good solution. However, the goal of this project is to investigate the various ways for choosing the inductor, considering both technical and economic convenience. Indeed, we must consider that usually the most performing solutions are the most expensive ones, and for commercialization of goods this means a decreased margin. Therefore, the designer must keep in mind the trade-off between top performances and prices.

For realizing an optimal choice of the core the designer can rely on many curves provided within the data sheet, among which the fundamental and empirical ones are :

- *The magnetization curve*, for relating induction and magnetic field in the core;

- *The core loss characteristics*, empirically computed by the manufacturer.

These two might also be present as set of curves, with different variables and different units of measurements, depending on the manufacturer and the country.

However, apart from these empirical curves, some key parameters are always provided within the data sheets for every inductor, due to the fact that their values are of great importance for understanding possible behaviors of the product. The main ones are:

Figure 4.2: Example of final toroidal inductor

- Permeability μ

- A_L, called inductance factor, the reciprocal of the reluctance $\mathcal{R}$

Hence permeability is the degree of magnetization that a material obtains in response to an applied magnetic field, while A_L is the obtained inductance with one-turn coil.

The algorithm used for evaluating the performance of a chosen core is now described, always based on the specifications reported for the planar inductor.

1. N, number of turns: the first step is the calculation of the number of turns needed for achieving the inductance necessary for the ZVS of the converter, based on the inductance factor of the selected core and the needed inductance. From the relation

$$L = A_L N^2$$

   we obtain that

$$N = \sqrt{\frac{L}{A_L}}$$

2. H, magnetic field: as previously stated in 2.1.2, knowing the number of turns with the relative peak current and the path length (L) of the core, by means of the Ampere's law

$$\oint_l H ds = N i_{peak}$$

   we can calculate H, which results to be

$$H_{peak} = \frac{N i_{peak}}{L}$$

3. B, induction: from the calculation of the H_{peak}, B can be evaluated using the characteristic magnetization curve of the material. Practically speaking, fitting curves are used so to compute numerically the real induction values. Depending of the catalog, instead of providing a B-H curve, it might be the case of a % μ-H curve, where the percentage of the initial permeability of the material is associated to each value of H. These curve might differ upon different conditions and materials.

4. Core losses: even in this case, the empirical curve is used with the corresponding fitting formulas to obtain numerical results, usually linking induction B and specific losses. Therefore, so to get the total losses of the component, the volume is involved, with

$$\text{Total losses} = \text{Specific losses} * \text{Volume}$$

5. ΔT: The temperature increase is usually given through an empirical function which depends on Core losses and dissipation surface, the latter being usually given on data sheets. It usually takes into account core coating for insulation purposes and wounded coil.

6. Feasibility: Once these numbers are obtained the feasibility of the system should be ascertained. The facts of being a good solution or not might depends on many factors. In this project, number of turns, ΔT and core losses were all strictly conditioned.

7. Price: it's well known that good performances are pricey. Even if feasible for the system, it might be economically not convenient, especially for medium/big scale production.

Although this is a linear algorithm for calculating the parameters of each inductor, it does not provide a way for evaluating the "goodness" of a solution with respect to the others. As a matter of fact, the key parameters of the cores are not direct function of a single variable, but rather a complex relation of variables involving non linear behaviors.

An example of this might clarify this concept, looking also at 4.3. Given a core with known characteristics, after having calculated its parameters by means of the previous algorithm, we suppose to increase its volume (**A**). On one hand, what we obtain is the increase of surface for heat dissipation(**B**), so diminished rise in temperature(**C**), probable increase of the path length(**D**) so decreased magnetic field H(**E**) and induction B(**F**), which would mean less specific losses(**G**), but on the other hand it also means more material, that means price increase(**H**), and even if the specific losses decrease, they have to be multiplied for the core volume, which was increased as root event(**I**). In conclusion, losses might remain unchanged, or even increase, despite the initial reasoning.

Therefore, there is no unique rule for varying the parameters so to improve the performances.
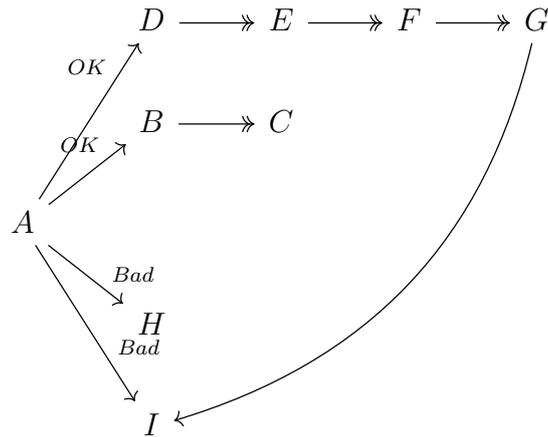
Figure 4.3: example of chain of events graphically depicted

4.1.1 No calculation approach

Beside providing the numerically most efficient solutions, it is helpful to provide an approach that might lead to a sufficiently effective solution without the need of a big amount of calculations.

The approach suggested in this thesis, which is not unique as well, is based on reasoning about permeability and dissipation surface.

After the choice of the material which behaves satisfactorily at high frequencies, given a B-H curve for that material at that band of frequencies, it can be approximated with a linear function as in Figure 4.4. Given that the more induction increases, the more specific
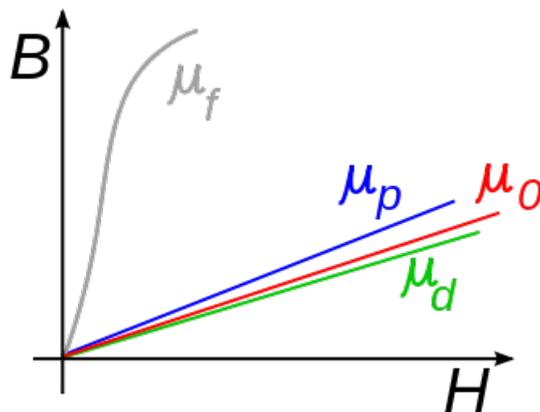
Figure 4.4: $B = \mu H$ characteristic for different values of permeability

losses grow, it might be worth choosing the core with the *smallest possible permeability*: in this way, even if at peak conditions the magnetic flux reaches high values, the induction module is still little. Moreover, the surface of a core is straightforwardly calculated from its dimensions, that are usually a given set of possibilities for each manufacturer: it might be said that molds have discretized surfaces, meaning that given a huge bunch of toroidal

inductor from the same provider, they can be divided in "few" groups of inductors having same dimensions and different materials. However, the set of possible surfaces tend to differ with non constant amounts. As a matter of fact, the number of medium-small sized inductor provided in catalogs is more than the big-sized ones, so that gaps between each measure are non-constant. Hence, while increasing the dimensions of the selected core, as soon as the surface leaps to a sufficiently good measure we might choose the one with lowest permeability, according to the previous reasoning. Wrapping up these concepts, the proposed design process consists of:

1. Choice of material, depending on electrical requirements;

2. Skim for cores with proper dissipating surface, according to the needs in terms of increasing temperature.

3. Choose the smallest and least permeable, which leads respectively to cost effectiveness (less material used) and less specific losses.

As already pointed, this "no calculation approach" that focuses on small values on permeability might lead to unsatisfactory results, for example knowing that small μ increase the possibility of leakage flux. Therefore, it has to e verified by means of simulations and/or tests. A practical design example in section 4.2, where the toroids from "Magnetics" are analyzed.

4.2 First manufacturer: Magnetics

"Magnetics" is a leading world supplier of precision soft magnetic components and materials to the electronics industry (from [3]). Due to the fact that the laboratory had previously purchased some components from this manufacturer, Magnetics catalog was the first one to be analyzed. A core catalog is usually organized in a fashion where the first section provides the knowledge that the designer needs to acquire for choosing the right solution, whereas the second section enlists core data according to dimensions, shape, etc.

Magnetics offers a wide variety of powder core solutions, with different shapes, dimensions and even materials. This last characteristic is particularly important in terms of inductor design, cause it is directly responsible for both the magnetic behavior of the component and for its cost, as well as for many other factors.

As far as Magnetics is concerned, 3 main type of materials are suitable for our requirements: MPP, HighFux and Kool Mu. As a matter of fact, "All Magnetics powder core materials are used in inductors, but each has its own advantages. For the lowest loss inductor, MPP material should be used since it has the lowest core loss. For the smallest core size in a DC Bias dominated design, High Flux should be used since it has the highest flux capacity. For reasonably low losses and reasonably high saturation at a

low cost, Kool Mu should be used since it has the lowest material costs". [4] XFlux option has not been considered since optimized for lower frequencies.
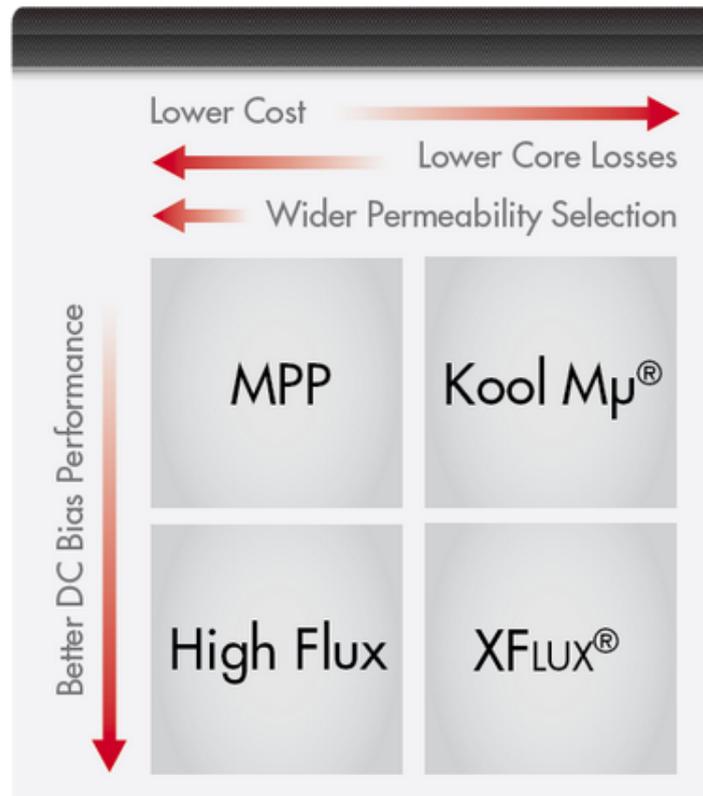
Figure 4.5: Magnetics table of materials for powder cores

First, the approach previously described is considered, returning a core model that is likely to satisfy our needs. After that, using the algorithm, the most efficient solution is determined by computations for each core.

4.2.1 No calculation approach on Magnetics

The first step is to check what is the most performing material for the converter frequency (100kHz), looking at the core loss curves and comparing them ([5], page 30 and following). Assuming small values of flux density (measured in Tesla in catalog), that is what we want to achieve by choosing little permeability, it can be noticed that at given small values of μ,the 100kHz line results in less losses for MPP cores with respect to other materials. For example, considering the smallest common permeability for the three materials (26μ) at 100kHz with Flux density of 0.01Tesla, the losses for the three materials are:

- MPP: around $3\frac{mW}{cm^3}$;

- High Flux: around $10.5 fracmW cm^3$;

- Kool mu: around $7\frac{mW}{cm^3}$;

Although MPP and Kool mu show a similar behavior for the flux in the example, the latter has a much steeper increase of losses while moving in the right part of the graph, which is likely to happen in practice due to the converter high peak current.

In addition, the only MPP material with lower permeability has $\mu = 14$, keeping in mind that we denote μ as the relative permeability of the material, so that

$$\mu_{tot} = \mu \mu_0$$

with μ_0 being the permeability of air. However MPP with $\mu = 14$ shows worse performances at low values of flux, as shown in figure 4.6, where at the same condition of the previous example, the core produces losses with density $6 \frac{mW}{cm^3}$ against the $3 \frac{mW}{cm^3}$ of the MPP $\mu = 26$ Therefore, the best choice with the lowest permeability results to be an MPP core with a total permeability of $26\mu_0$.

The next step is to choose, among the MPP $\mu = 26$ cores, the smallest one in terms of volume with the biggest surface area. More precisely, the minimum surface needed for dissipating the losses of the component might be estimated by making use of the relation (see [5], page 11)

$$\Delta T = (\frac{\text{Losses}[mW]}{\text{Surface Area}[cm^2]})^{0.833}$$

it might be asserted with a reasonable degree of certainty that losses might be around 5W, with a possible increase in temperature of 15°C. If so, by means of the equality

$$\text{Surface Area}[cm^2] = \frac{\text{Losses}[mW]}{\Delta T^{\frac{1}{0.833}}}$$

we obtain a rough value for the surface area of 190cm². Skimming for components with similar surfaces, according to the catalog, the cores with outer diameters (OD) close to 60cm comply with that requirement. In figure 4.8, data of possible inductors with similar diameter are provided.

It might be noticed that the surface does not have the same increasing trend as the diameter, trivially caused by the square or the radius present in the calculation of the area of the circle, being the toroidal volume built by revolution from a rectangular surface. Reasoning about the Table 4.8, the 2nd row has an unsatisfactory surface, which would yield too high temperatures inside the charger; neither the 3rd row is good for our purposes, cause even the volumes increase by the squared radius, which would mean more material used so a too high cost per unit. Differently, the solution with $OD = 62$cm have a more than sufficient surface while having a good volume.

In conclusion, this approach addresses the component **55615** (see [5], page 82) as a good solution to our needs. The verification of this result will be at the end of the next section, where calculations will prove its effectiveness.

MPP 26μ

$$P_L = 70.83 B^{2.34} f^{1.65}$$

High Flux 26μ

$$P_L = 374.9 B^{2.21} f^{1.49}$$

Kool Mμ® 26μ, 40μ

$$P_L = 120 B^{2.09} f^{1.46}$$
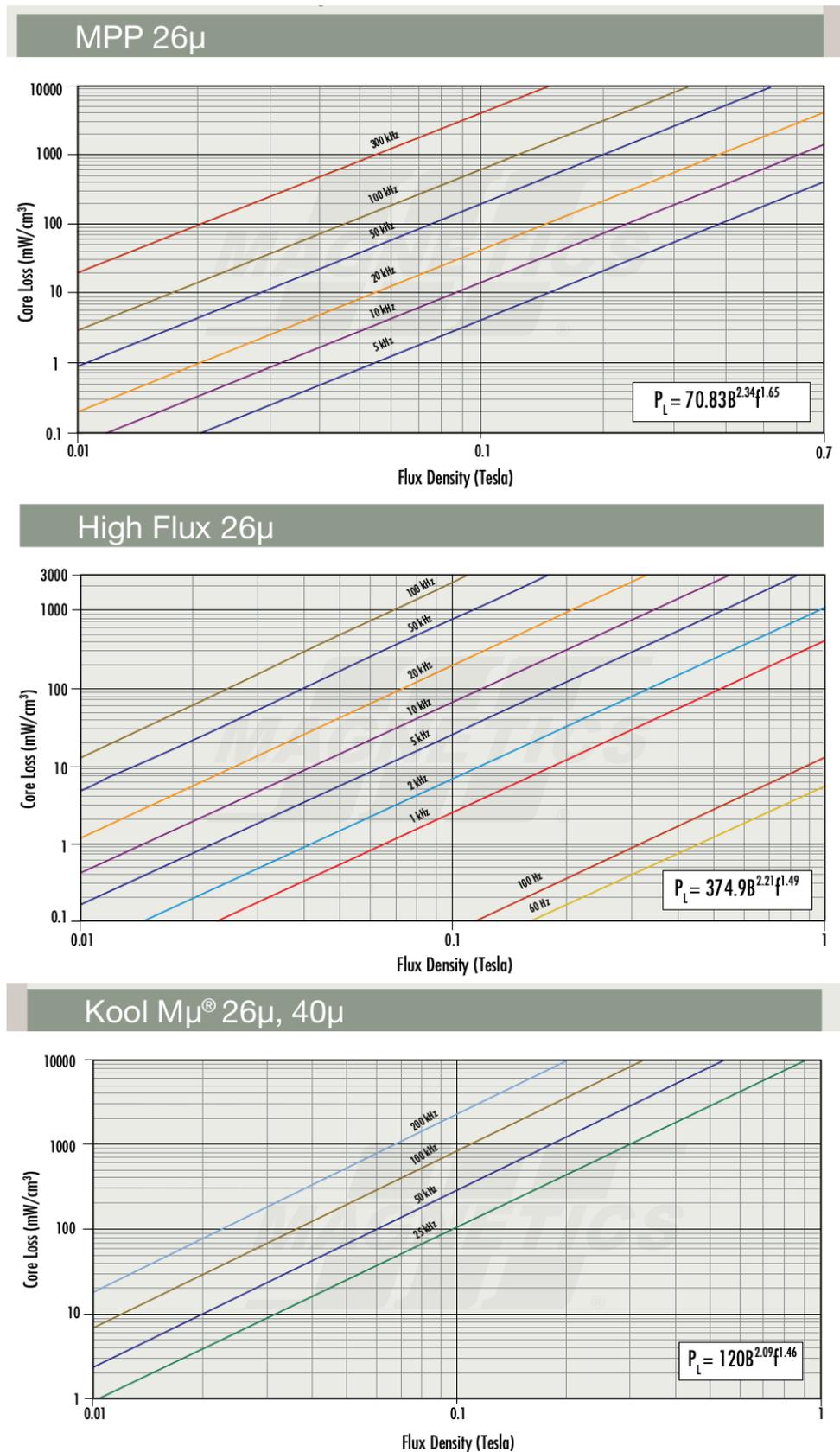
Figure 4.6: Comparison of Core losses among materials
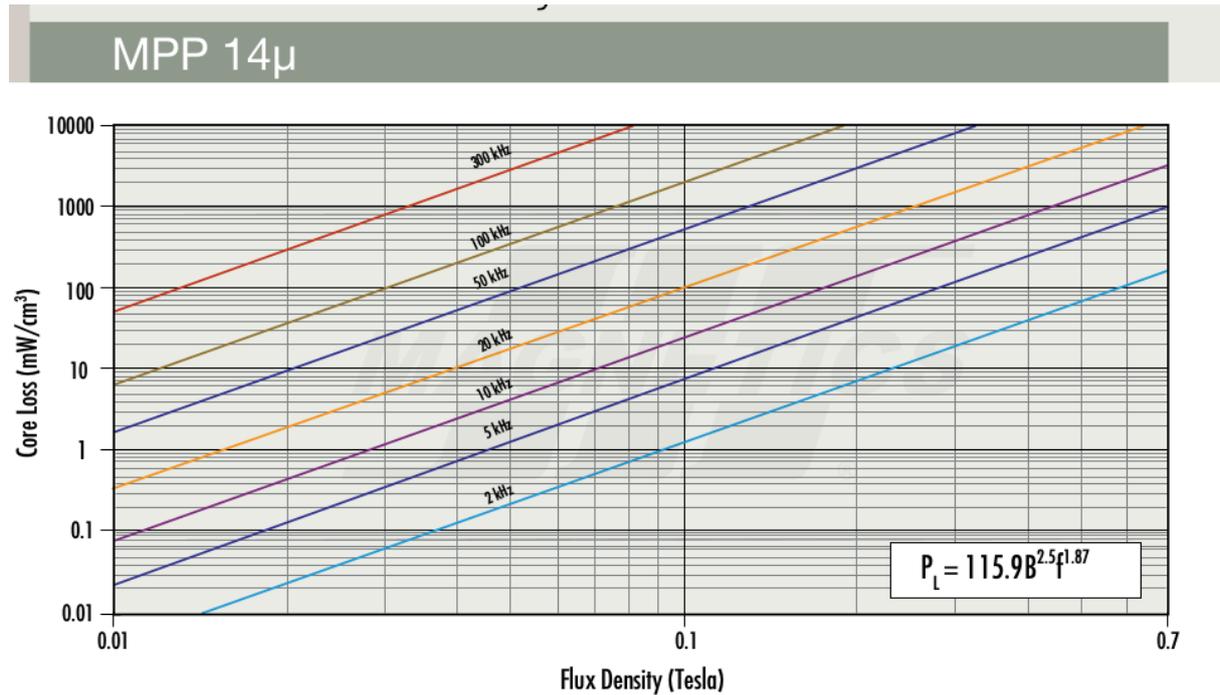
Figure 4.7: MPP μ14 Core Losses versus Field Density

Outer Diameter [cm]	Surface (40% winding factor) [cm^2]
50.8	110
57.2	120
62	210
74.1	330

Figure 4.8: list of possible candidates

4.2.2 Algorithm for parameters calculation on Magnetics

An example of calculations for estimating the real behavior of a toroidal inductor is now going to be made. This might be seen both as a simulation for choosing a component comparing results from a group, and as a proof for testing the behavior of the chosen inductor.

Following the steps in 4.1, we test the part number **55615**, found following the way of thinking of 4.2.1.

1. N, number of turns:

$$N = \sqrt{\frac{L}{A_L}} = 10.3 \rightarrow = 11$$

   with $L = 8\mu$H, $A_L = 82$H, but a value decreased of 8% has been used under manufacturer suggestion, so to consider the worst case scenario;

2. H, magnetic field:

$$H_{peak} = \frac{Ni_{peak}}{l} = \frac{11 * 21\text{A}}{1.44\text{cm}} = 16\text{A}* \text{ Turns }/\text{cm}$$

3. B, induction: From the B-H curve for MPP with permeability $\mu = 26$(see [5], page 39), we can roughly evaluate the inductance with a certain error. For a precise calculation, the fitting formula is needed (see [5], page 41)

$$
\begin{aligned}
B &= \left(\frac{a + bH + cH^2}{1 + dH + eH^2}\right)^x \\
&= \left(\frac{6.68E - 02 + 1.11E - 02 * 16 - 1.14E - 05 * 16^2}{1 + 1.11E - 02 * 16 - 1.23E - 05 * 16^2}\right)^2 = 0.042\text{T}
\end{aligned}
$$

where these parameters depend on material and permeability.

4. Core losses: Looking at the core losses curve for MPP with $\mu = 26$ (4.6), and using the fitting formula

$$
P_{LDensity} = 70.83 * B^{2.34} f^{1.65} = 70.83 * 0.042^{2.34} * 100000^{1.65} = 85.3\frac{mW}{cm^3}
$$

where B is the inductance and f the current frequency. Therefore, the total losses are

$$
P_{\text{LTotal}} = P_{\text{LDensity}} * \text{Volume} = 4.42W
$$

where volume has been calculated multiplying cross section for path length.

5. ΔT:
$$
\Delta T = \left(\frac{\text{Losses}[mW]}{\text{Surface Area}[cm^2]}\right)^{0.833} = \left(\frac{4.42 * 1000}{120}\right)^{0.833} = 20.18°\text{C}
$$

The increase in temperature seems too high with respect to the boundary of 15°C considered as upper limits for choosing the component, but indeed the result obtained here is the worst case scenario, where the surface used for calculation was the unwound one instead of the 40% winding factor one. The most unlucky case should always be considered for sizing components, so that the practical behavior of the real component under test is always satisfactory, independently from the conditions.

6. Feasibility: The two criteria used for judging the feasibility of the system were

   - $N < N_{MAX}$ considering a winding factor of 40% and the window area of the core

   - $\Delta T < 60°\text{C}$

   for 55615, both conditions were satisfied, making it a feasible solution.

7. Price: Magnetics' solutions are not cheap, therefore for the sake of economy a differen provider might be considered.

These results ensure the theoretical effectiveness of the core selected by means of the so called "no calculation" approach: 55615 respects indeed all the requirements, which confirms it as a candidate ready to be tested inside the real converter.

This whole calculation process applies for each of the 3 materials (MPP, HighFlux, KoolMu) and outputs the parameters from which the designer is able to judge whether a component might be purchased or not.

A procedure that might improve the behavior of a single core in terms of dissipation of heat is the *"stacking"*, which means literally to stack two or more cores one over the other, wounding coils as if the stack was a single bigger core. This clearly increases the dissipation surface, but also the total volume of metallic material. As it has been discussed in 4.3, both pros and cons come from this implementation, which might or might not be worth.

Indeed this whole process has been implemented for each component in the Magnetics catalog. Although it was time consuming, the use of an electronic sheet such as Excel made it easier and more clear, showing that there are cores that, under the same conditions as before, behave better than 55615, which however results to be in the top five in terms of losses. This fact stresses again that many ways of thinking might suit a designing process, and that the one presented in this thesis was able to select a good solution, even if the most optimized. Beside single cores, a possible stack of 2 identical cores has been considered in the calculation process, taking care of modifying cross section, A_L and consequently total surface and total volume accordingly.

A bunch of few components were selected from these calculations for each material, both single and stacked, as shown in the table 4.1. For the sake of clarity, only the most important design parameters are shown, with a precision of two decimals. The real Excel table includes more parameters with higher precision.

Moreover, it might be interesting to analyze what are the similarities between the feasible components, looking for a distribution trend by means of plots. In this case, MPP feasible cores are covered, with permeability versus dimensions graphs.
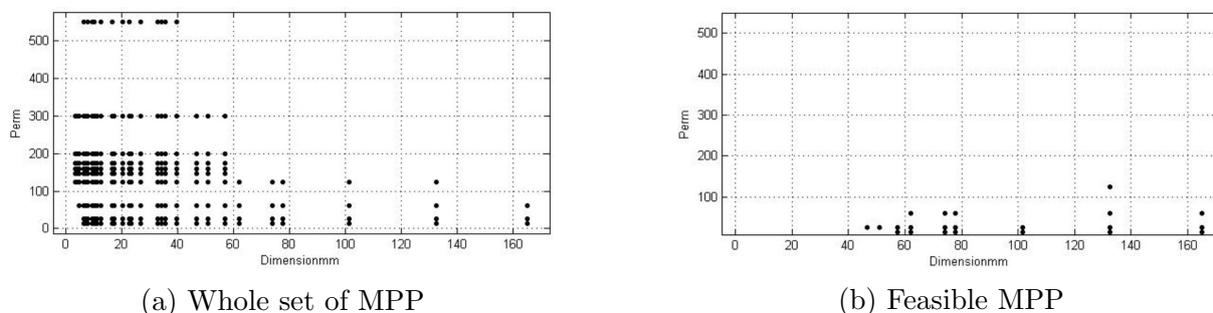

(a) Whole set of MPP

(b) Feasible MPP

Figure 4.9: Feasible component distribution in Permeability/Dimension plane

It is indeed true that for low values of permeability, losses tend to decrease, as can be observed comparing the distribution of feasible cores (Figure 4.9b) with respect to the

Table 4.1: Selected compliant inductor from Magnetics

MPP (single)

Part Num	OD(mm)	Perm. μ	AL	PathLenght(cm)	CrossSec(cm2)	N	Hmax(AT/cm)	B(T)	PL density	PL TOT(W)	Surface(cm2)	ΔT	Feas #turns	Adopt?
55735	74,10	26,00	88,00	4,97	1,84	10	11,41	0,03	35,48	3,24	190,00	10,63	49,34	YES
55615	62,00	26,00	82,00	3,60	1,44	11	16,04	0,04	85,31	4,42	120,00	20,18	25,11	YES
55868	77,80	26,00	30,00	1,76	1,96	18	19,29	0,05	139,33	4,81	110,00	23,25	57,93	YES
55191	57,20	26,00	60,00	2,29	1,25	13	21,84	0,06	194,59	5,57	85,00	32,59	16,36	YES

MPP (stack of two)

Part Num	OD(mm)	Perm. μ	AL (x2)	CrossSec(cm2)	CrossSec(cm2)	N	Hmax(AT/cm)	B(T)	PL density	PL TOT(W)	Surface(cm2)	ΔT	Feas #turns	Adopt?
55908	77,80	26,00	74,00	4,42	1,96	11	11,79	0,03	38,46	3,33	198,03	10,50	57,93	YES
55735	74,10	26,00	176,00	9,94	1,84	8	9,13	0,02	20,64	3,77	326,91	7,67	49,34	YES
55615	62,00	26,00	164,00	7,20	1,44	8	11,67	0,03	37,49	3,89	200,40	11,82	25,11	YES

HighFlux(single)

Part Num	OD(mm)	Perm. μ	AL	CrossSec(cm2)	CrossSec(cm2)	N	Hmax(AT/cm)	B(T)	PL density	PL TOT(W)	Surface(cm2)	ΔT	Feas #turns	Adopt?
58734	74,10	14,00	48,00	4,97	1,84	14	15,98	0,01	6,87	0,63	190,00	2,71	49,34	YES
58614	62,00	14,00	44,00	3,60	1,44	15	21,88	0,02	40,62	2,11	120,00	10,87	25,11	YES
58735	74,10	26,00	88,00	4,97	1,84	10	11,41	0,01	28,33	2,59	190,00	8,81	49,34	YES

HighFlux(stack of two)

Part Num	OD(mm)	Perm. μ	AL (x2)	CrossSec(cm2)	CrossSec(cm2)	N	Hmax(AT/cm)	B(T)	PL density	PL TOT(W)	Surface(cm2)	ΔT	Feas #turns	Adopt?
58869	77,80	14,00	28,00	3,52	1,96	18	19,29	0,01	20,70	1,43	172,46	5,82	57,93	YES
58909	77,80	14,00	28,00	4,42	1,96	18	19,29	0,01	20,70	1,79	198,03	6,27	57,93	YES
58112	57,20	14,00	28,00	2,88	1,43	18	26,43	0,03	103,34	4,26	120,82	19,43	30,18	YES

KoolMu(single)

Part Num	OD(mm)	Perm. μ	AL	CrossSec(cm2)	CrossSec(cm2)	N	Hmax(AT/cm)	B(T)	PL density	PL TOT(W)	Surface(cm2)	ΔT	Feas #turns	Adopt?
77908	77,80	26,00	37,00	2,21	1,96	16	17,14	0,07	338,14	14,65	130,00	51,19	57,96	YES
77615	62,00	26,00	82,00	3,60	1,44	11	16,04	0,06	302,76	15,69	120,00	57,96	25,11	YES
77735	74,10	26,00	88,00	4,97	1,84	10	11,41	0,05	175,29	16,03	190,00	40,23	49,34	YES

KoolMu(stack of two)

Part Num	OD(mm)	Perm. μ	AL (x2)	CrossSec(cm2)	CrossSec(cm2)	N	Hmax(AT/cm)	B(T)	PL density	PL TOT(W)	Surface(cm2)	ΔT	Feas #turns	Adopt?
77908	77,80	26,00	74,00	4,42	1,96	11	11,79	0,05	184,29	15,97	198,03	38,73	57,96	YES
77615	62,00	26,00	164,00	7,20	1,44	8	11,67	0,05	181,39	18,81	200,40	43,96	25,11	YES
77616	62,00	40,00	252,00	7,20	1,44	6	8,75	0,05	201,19	20,86	200,40	47,92	25,11	YES
77735	74,10	26,00	176,00	9,94	1,84	8	9,13	0,04	124,93	22,85	326,91	34,39	49,34	YES

whole set of Magnetics' core (Figure 4.9a). In addition, the fact of considering bigger cores leads to both higher losses and better dissipation (4.3), that in this case makes the components feasible. This fact is underlined by the plot where the ΔT is introduced as third axis, in Figure 4.10
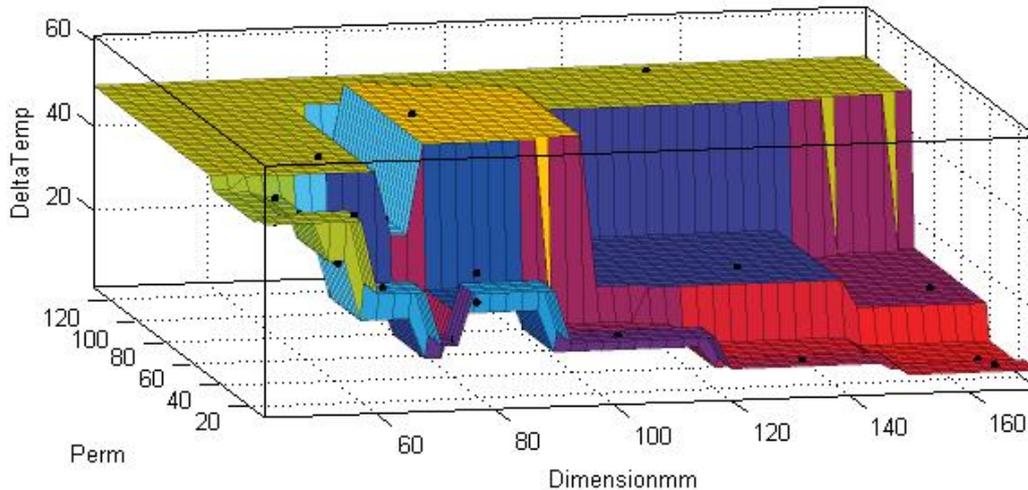

Figure 4.10: Distribution introducing the third axis ΔT

Now another manufacturer is going to be considered, but for the sake of completeness the proposed method is going to make use of their proprietary design tool, where the effectiveness of the cores in output is going to be verified by means of the algorithm already implemented for Magnetics' products (see 4.1).

4.3 Second Manufacturer: Micrometals

This second manufacturer has been suggested for its lower costs, with respect to Magnetics, which might suggest little worsen performances of its components. The designer should keep in mind that this project targets the improvement of performances, therefore less costs become advantages as long as *minimum requirements* are respected, meaning that the trade off between costs and quality must tend toward quality.

From Micrometals both single and stacked solutions are going to be considered, addressed by their proprietary software "MicroReleaseMarch2010.exe" (see [6]).

The task of this section is the description on those solutions, verifying the results by means of the calculation process used in 4.1.

Among Micrometals' solutions, "the iron powder group for power application covers materials with permeabilities from 10 to 100 intended for frequencies ranging from line frequency to 5MHz. Core sizes range from .14 inches (3.4mm) to 6.5 inches (165mm) with an extensive selection of shapes including toroids, E-cores, U-cores, bus bar cores, hollow cores, plain cores, pot cores and pot core assemblies. "(see [7]).

For this project, toroids need to be tested for finding a possible contender against the planar inductor described in chapter 2. More in particular, among the different kind of powders, "the low permeability of materials -2/-14 will result in lower operating AC flux density than with other, with no additional gap-loss. The -14 Material is similar to -2 Material with slightly higher permeability", as depicted in the catalog for Power Conversion and Line Filter Applications (see [8]). Therefore, the same strategy used for Magnetics will be followed, trying to choose components with small permeabilities for achieving small inductions.

Now the process is going to be described.

4.3.1 The design tool from Micrometals

The tool user interface comprises a wide set of options, among which for the purpose of this design the "60Hz" button is needed, in the "toroid and E cores" column (Figure 4.11a). Then, the requirements have to be indicated, as shown in figure 4.11b: these are obviously the same as the ones for Magnetics toroids and for planar inductor. It might be worth to notice that the tool asks for the RMS value of current instead of the peak one.
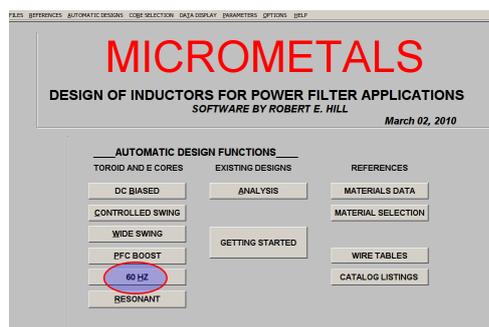
(a) Software front page
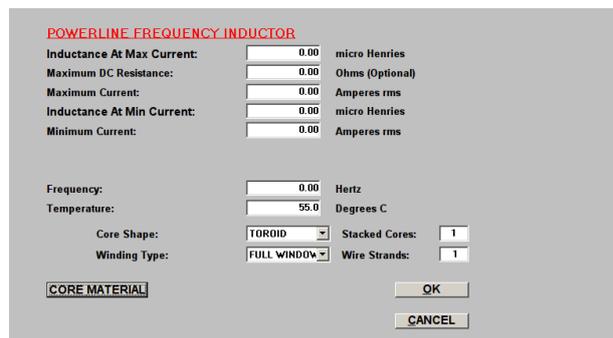
(b) Software data input

Figure 4.11: Micrometals Tool GUI

As reported in figure 4.11b, a single core solution is firstly investigated, while for a stack of two the designer just needs to modify the number labeled as "Stacked Cores". These were the few steps for having an answer from the tool, that now provides the designer with many possible solutions. It's interesting to notice that all the found solution are of the -2/-14 material type, the suggested type since the very beginning, even if the core type was not a specified requirement. The material is denoted by means of the second number after the letter 'T' in a core part number, as described in Figure 4.12.

The results from the tool have been tabulated in Figure 4.2.

It might immediately be noticed that the performances of these component are quite worse with respect to Magnetic ones, even if most of them respect the requirements of the project in terms of losses and temperature increase. Moreover, considering the smallest

Table 4.2: Results from Micrometals

Single Core CorePartNumber	Price	AL nH	Turns	WireAWG	%Fill	RdcOhms	BacGauss	%Perm	CoreLossWatts	CopperLossWatts	TempRisedegC
T200-2B	2,58	22	19	#5	40,2	2.11m	429,2	100,0	7,34	0,61	32,3
T225-2	1,79	12	26	#6	34,6	2.62m	528,2	100,0	7,92	0,76	37,1
T225-2B	3,22	22	19	#4	40,2	1.77m	379,2	100,0	7,01	0,51	26,4
T225-14B	4,09	28	17	#4	35,9	1.47m	441,8	100,0	10,40	0,43	35,7
T250-14	6,16	43	14	#4	37,4	1.34m	376,9	100,0	11,20	0,39	33,8
T300-2	2,84	11	26	#3	36,7	1.60m	424,2	100,0	7,89	0,46	23,1
T300-2D	5,63	23	19	#1	42,7	1.10m	308,1	100,0	7,83	0,32	18,2
T300-14D	7,13	28	17	#1	38,2	884u	338,6	100,0	10,27	0,26	22,6
T400-2	7,23	18	21	#1	34,7	1.05m	262,7	100,0	7,06	0,30	13,4

| Stack of two cores CorePartNumber(#Stacked)	Price	AL nH	Turns	WireAWG	%Fill	RdcOhms	BacGauss	%Perm	CoreLossWatts	CopperLossWatts	TempRisedegC
T175-2x2	1,31	30	16	#6	36,7	2.37m	430,6	100,0	7,36	0,68	35,1
T184-2x2	1,82	48	13	#6	37,8	2.14m	399,0	100,0	8,74	0,62	36,5
T200-2x2	1,44	24	18	#5	38,1	2.04m	408,9	100,0	7,23	0,59	30,9
T200-2Bx2	2,58	44	14	#4	37,4	1.84m	316,3	100,0	7,48	0,53	23,9
T225-2x2	1,79	24	18	#4	38,1	1.70m	365,7	100,0	7,10	0,49	25,8
T225-2Bx2	3,22	43	14	#3	37,3	1.51m	279,4	100,0	7,10	0,44	19,7
T225-14Bx2	4,09	56	12	#2	40,3	1.06m	311,9	100,0	9,68	0,31	24,1
T250-14x2	6,16	86	10	#2	42,5	955u	269,2	100,0	10,61	0,28	23,4
T300-2x2	2,84	23	19	#1	42,7	1.10m	310,0	100,0	7,89	0,32	18,4
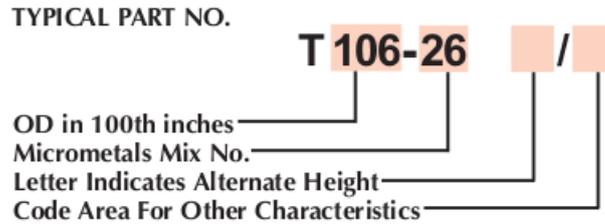
Figure 4.12: Part-number meaning

components among the resulting ones, the core **T200-2B** appear as good candidate for both single and stacked solutions, with satisfactory behaviors. It should be pointed that the letter 'B' inside the name stands for a different height with respect to the standard T200-2. Other useful information provided by the tool are the temperature rise with respect to worked hours, which sets an ideal time limit after which performances degrade till a new piece is needed, and the inductance provided by the inductor with respect to the current, that in our conditions is almost fixed to the desired value of 8µH. Both of them are shown in Table 4.13.
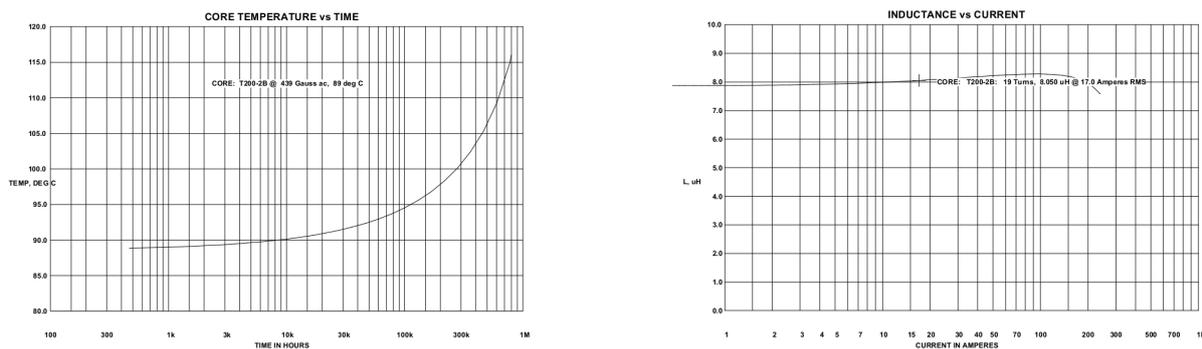

Figure 4.13: Additional information from the tool

Looking at the catalog, the main characteristics of the component T200-2B are:

- $A_L[\frac{nH}{N^2}] = 21.8$;

- $\mu = 10$ according to the figure 4.14, that for type -2 materials remains almost constant even at much higher frequencies than 100kHz; ;

- path length: 13cm;

- cross section: 2.32cm^2;

- volume: 30cm^3.

In the following a performances verification is going to be proposed under single core configuration, using the calculation process previously adopted and the tool references.
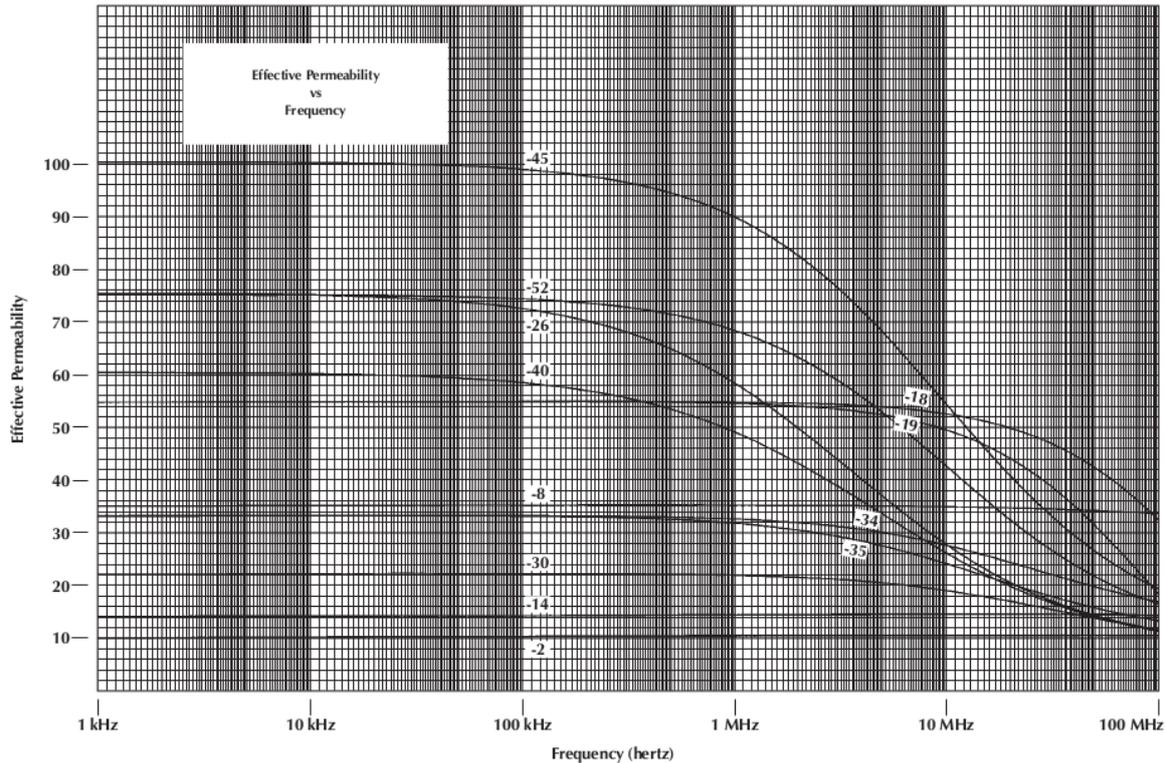
Figure 4.14: Effective permeability vs frequency

4.3.2   Algorithm for parameters calculation on Micrometals

1. N, number of turns:

$$N = \sqrt{\frac{L}{A_L}} = \sqrt{\frac{8}{22 * 0.95}} = 19$$

   with $L = 8\mu H$, $A_L = 22H$, but a value decreased of 5% has been used so to account for worsen scenarios;

2. H, magnetic field: Due to different conventions in terms of unity of measure, the magnetic field is addressed using "Oersted", where:

$$1Oe = 0.7958A/cm$$

   The reason for this choice, apart from being cultural, depends on the way to treat the vacuum permeability μ_0. From the European point of view, μ_0 is the constant that, multiplied for the relative permeability μ (the one that has been considered along the whole paper) results in the total permeability. Conversely, Americans and others consider the vacuum permeability together with the magnetic field H, that due to the constant value

$$\mu_0 = 4\pi * 10^{-7} \frac{N}{A^2}$$

   is like changing H's unity of measure (exactly Oersted "Oe").In this way, μ_0 disap-

pears from the relation of H and B:

$$B = \mu_0 \mu H [\frac{A}{m}] = \mu_{TOT} H [\frac{A}{m}] = \mu H [Oe]$$

On the other hand, the new expression for H is

$$H_{peak} = \frac{0.4 \pi N i_{peak}}{l} = \frac{0.4 * \pi * 19 * 21}{13} = 38.6 \text{Oe}$$

3. B, induction: From the B-H curve provided within the catalog the designer is only able to approximately judge the kind on magnetic material handled (Figure 4.15). For a precise induction calculation, the designer might use the permeability with
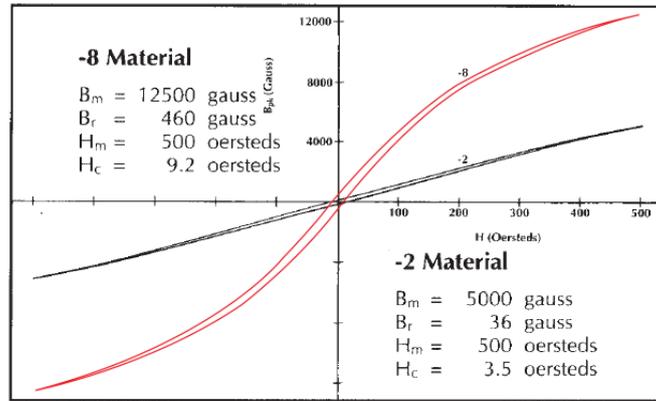

Figure 4.15: BH curve

the previously calculated magnetic field. However, an issue occurs, due to the fact that permeability changes with respect to the working conditions. By means of a graph provided in the catalog, and reported in Figure 4.16, and the reported rough formula for B_{pk}, the real percentage of the initial permeability can be evaluated and compared with the value provided by the tool as follows:

$$B_{pk} = \frac{E_{rms} 10^8}{4.44 * \text{CrossSec} * N * \text{freq.}} = 615\text{G}$$

where $1\text{T} = 10000\text{G}$. Without the need of an adaptive formula for the -2 type curve, the designer can easily appreciate an increase of few percents $(+1\% - 2\%)$, as reported in the electrical analysis of the T200-2B from the tool (Figure 4.16).

Therefore, it follows that

$$B = \mu H [Oe] = (10 + 1) * 38.6 = 425 \simeq 430\text{G}$$

which *confirms* the result provided by the tool.

```
CORE PART NUMBER        T200-2B    X  1   NUMBER IN STACK
WIRE GAGE               # 5 AWG    X  1   STRANDS
NUMBER OF TURNS              19
AC CURRENT               17.00         AMPERES RMS
FREQUENCY            100000.00         HERTZ
AMBIENT TEMPERATURE       55.0         DEGREES C


ELECTRICAL PROPERTIES:

INDUCTANCE          8.05 u    Henry    CORE LOSS          7.72      W
DC RESISTANCE       2.11 m    OHMS     COPPER LOSS        0.611     W
AC RESISTANCE                 OHMS     BUILD              0.308     in.
RIPPLE CURRENT              AMPS p-p   SURFACE AREA       122.6     Sq cm
DC BIAS                       OES      TEMP RISE @ 0 HRS  33.6      DEG C
AC FLUX DENSITY        439    GAUSS    Time To 115 % Loss 4.65e+04  Hours
PERCENT PERM           102    PCT      Life Limit         8e+05     Hours
CORE AL VALUE           22    nH
```

Figure 4.16: From Tool, electrical analysis of T200-2B

4. Core losses: For the losses calculation, the catalog provides designer with both plot density losses versus peak flux density (Figure 4.17) and the relative fitting formula (see [8], pag 30 of the pdf), from which the precise value is obtained.

$$CL(mW/cm^3) = \frac{f}{\frac{a}{B^3} + \frac{b}{B^{2.3}} + \frac{c}{B^{1.65}}} + (df^2B^2) = ... = 244\text{mW/cm}^3$$

Total losses are just the multiplication of density for the volume of the core, provided within the data-sheet.

$$\text{TOT Losses} = CL * \text{Volume} = \frac{244 * 30}{1000} = 7.32\text{W}$$

which is, as expected, very close to the tool result.

5. ΔT: Since the Micrometals' catalogue does not provide a computation way for testing the increase in temperature, apart from the tool, the designer might make use of the fitting formula within Magnetics catalog, in order to roughly judge the correctness of the software. Therefore, after a trivial computation of the dissipation surface by means of the geometrical parameters of the core:

$$\Delta T = (\frac{\text{Losses}[mW]}{\text{Surface Area}[cm^2]})^{0.833} = (\frac{7.32 * 1000}{90.74})^{0.833} = 38.75°\text{C} \simeq 32°\text{C}[FromTool]$$

Indeed the correctness of the software has been assured for a single stack implementation, which lets the designer suppose that it would yield true results even for stacked cores and for other kind of inductors.
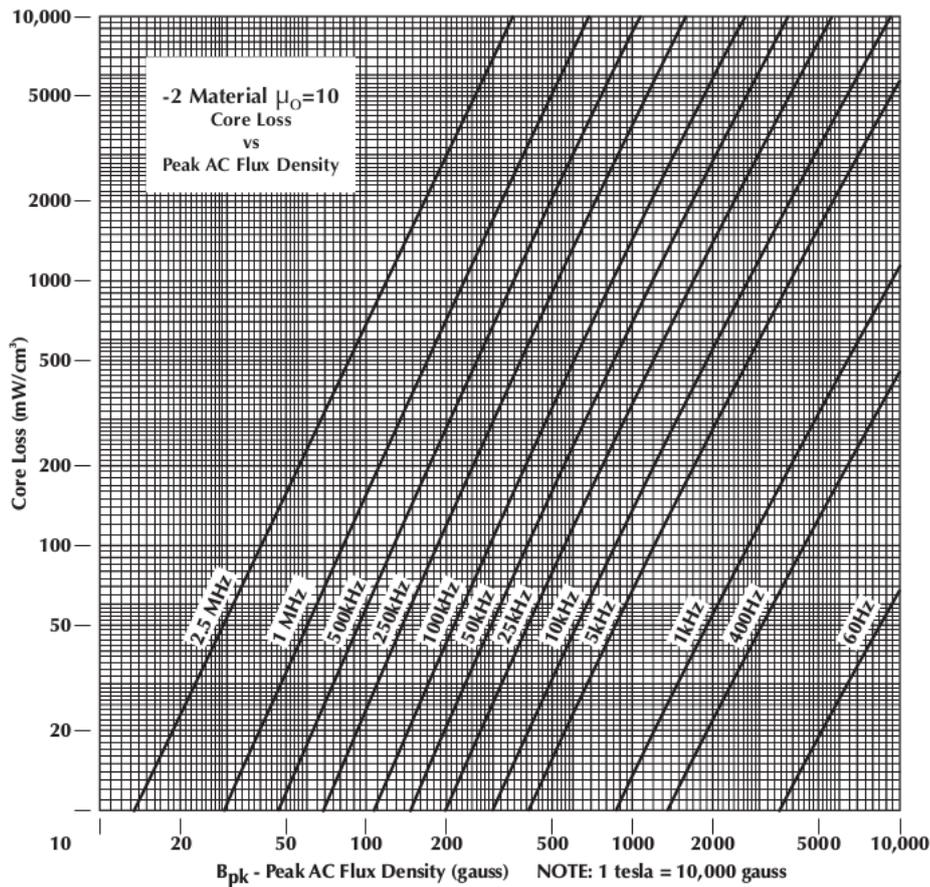
Figure 4.17: 2 type core losses vs peak flux density, function of frequency

In conclusion of this section, few further considerations about the results from Micrometals:

- As has already been pointed, the letter 'B' in the name of the component means that its height is different from the one without 'B', that in the case of T200-2B and T200-2 doubles the height. A curious but predictable result is that, comparing the behavior of a stack of two T200-2 and a single core T200-2B from the table 4.2, the parameter are almosts the same for both.

- From the results of this chapter, it might be the case that a toroidal configuration could substitute a planar one, judging upon the performances under simulation. The real test will be described in Chapter 4, where the component will be under test for nominal and stressful conditions. Moreover, before tests on the real product, the next section investigates possible winding arrangement along with the magnetic simulations of the toroidal inductor.

4.4 Windings arrangements and simulations

At these working frequencies, the impact on the overall performances of the system are heavily affected by skin and proximity effects, as discussed in Chapter 2.

As far as skin effect is concerned, its impact on the conductive materials present in the system can be evaluated by means of a parameter called *skin depth*, denoted by δ and approximated as follows:

$$\delta = \sqrt{\frac{2\rho}{\omega\mu}}$$

where ρ = resistivity of the conductor, ω = angular frequency of current = $2\pi*$frequency, μ = permeability. Regarding a copper wound object, the skin depth for this material results to be

$$\delta = \frac{7.4}{\sqrt{\text{frequency}}}\text{cm} = 0.2\text{mm}$$

Therefore, a huge wire does not contribute neither to an efficient behavior of the component nor to a cost-effective solution, leaving a variable but consistent percentage of copper unused. At the same time, a smaller active section of copper leads to higher current densities, which worsen the system. According to this reasoning, a Litz wire composed on many thin wires with a diameter smaller than the skin depth would yield a more homogeneous current distribution, increasing the active copper section and consequently the performances.

In order to show this, it has been consider the 55735 from Magnetics, found to be the best solution from the catalog (see 4.1) wound with copper wire with a diameter $d = 4$mm, purposely bigger that the one needed so to stress the effects of different implementations on the system. However, for the losses calculation in Femm of the toroidal solutions, both 55735 and T200-2B are going to be considered, simulated with wire having equivalent section of the planar inductor.

The specifications of the ferrite are:

- Permeability $\mu = 26$;

- Number of turns N=10;

- Outer diameter OD = 75mm;

- Inner diameter ID = 44mm

Moving from one simulation to the other, the physical number of turns will increase and the relative consequences analyzed. However, in order to maintain unchanged the electromagnetic contribution of the inductor inside the system, comparing the results of one implementation with respect to the others, the equivalent number of turns with nominal current will be constant: what will change is the number of windings in parallel

for each turn, where the copper used in the initial configuration for each turn will be distributed among the wires in parallel. *Thus, the total copper section per turn is constant for each of the following simulations* (considering the aforementioned wire, $A = \frac{d^2\pi}{4} = 4\pi$mm) and the total number of windings will be a multiple of 10, depending on the chosen parallelism. This leads also to a approximately *constant DC resistance* of the wire, so to obtain a feasible comparison.

The higher is the parallelism, the more visible the Litz benefits on the system become, but for the sake of clear drawing the largest simulated parallelism is 4, with $4 * 10 = 40$ turns. Thus, the chosen physical number of turns are 10, 20, 30, 40.

In the following figures, the range of colors has been assigned in each case based on the same upper bound, so to appreciate the different color distribution depending on the parallelism. Flux lines are enhanced as well. The lines crossing the copper section in the zoomed pictured have been used to plot the distributions by means of Matlab software.
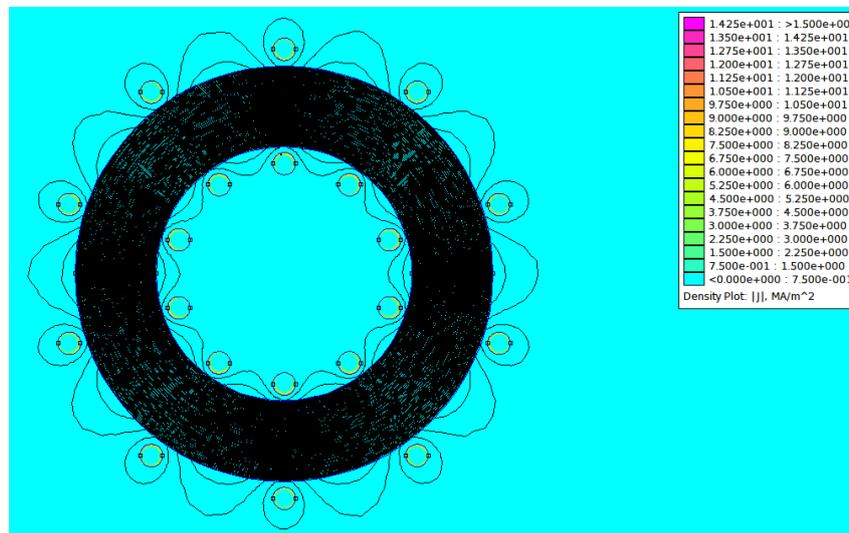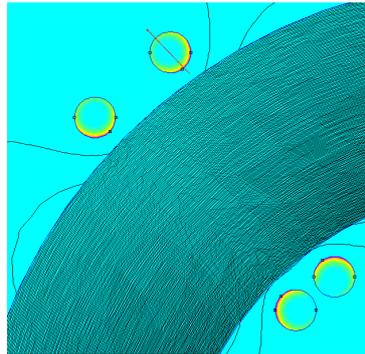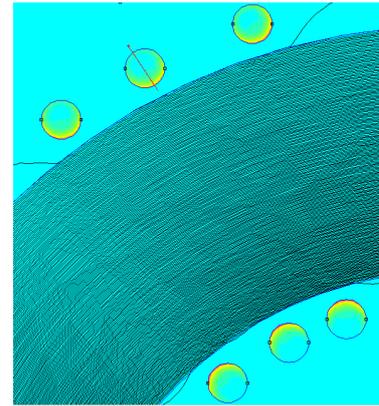

(a) 10 windings, parallelism=1
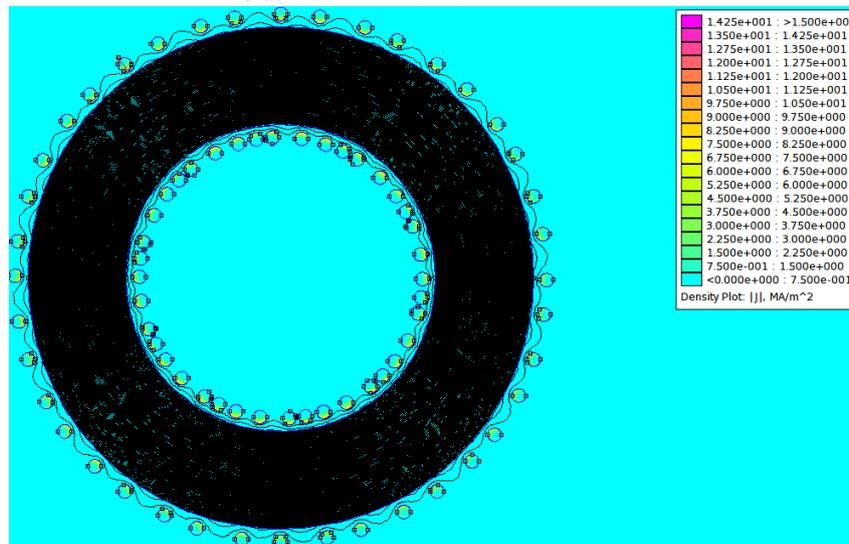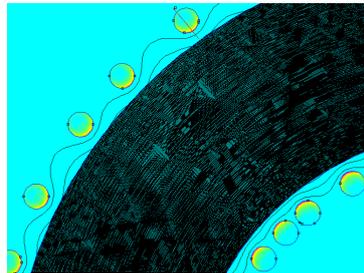

(b) 40 windings, parallelism=4
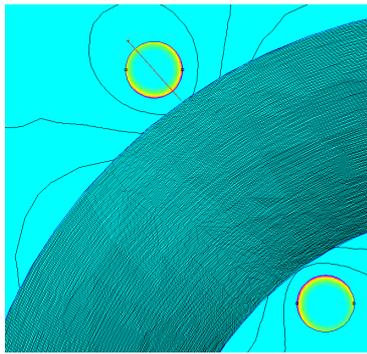
(a) 10 windings, parallelism=1, ZOOMED

(b) 20 windings, parallelism=2, ZOOMED

(c) 30 windings, parallelism=3, ZOOMED


(d) 40 windings, parallelism=4, ZOOMED

The orientation of the x-axis is so that the more x increases, the closer the considered point is to the ferrite. The main considerations about the current density distribution along a diameter (4.20a) and the flux lines distribution are:

1. The first thing to be noticed from the graphs is that the diameter of the wire does not decrease linearly: as a matter of fact, being the total section constant, the diameter evolves as a square root, more precisely

$$d = \sqrt{\frac{S}{n\pi}}$$

where n is the parallelism (in our simulations, $n \in \{1, 2, 3, 4\}$) ;

2. Peak values of current density are achieved at the edges of the conductor, as it was expected from the theory of skin effect. Conversely, the midpoints present the smallest values in each of the four curves;

3. Looking at the zoomed graph for the central area of the wire (4.20b), it might be noticed that the average current density for those points increases as the parallelism increases. This trend is confirmed by the Figure 4.20 where the geometrical center of the circumference is considered;

4. Regarding the first extremity around $x \approx 1$mm, the comparison between graphs
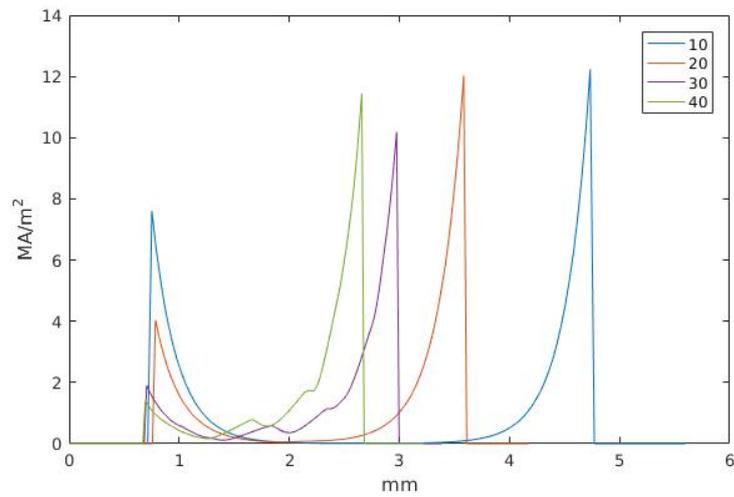
(a) Current density distribution along a diameter
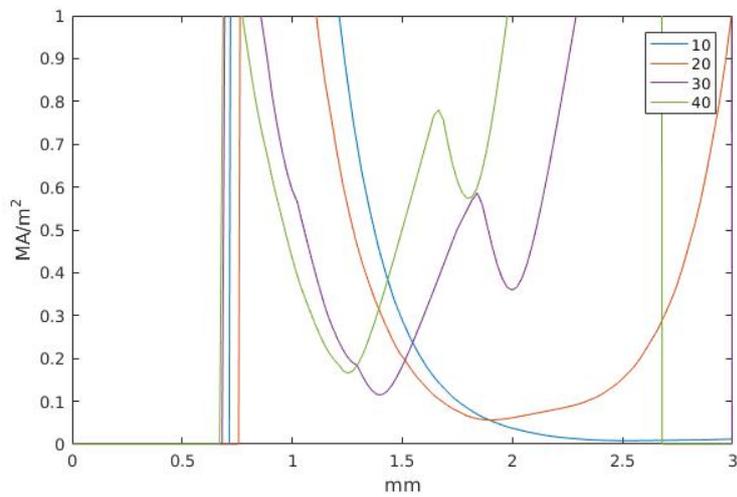
(b) Current density distribution along a diameter, ZOOMED

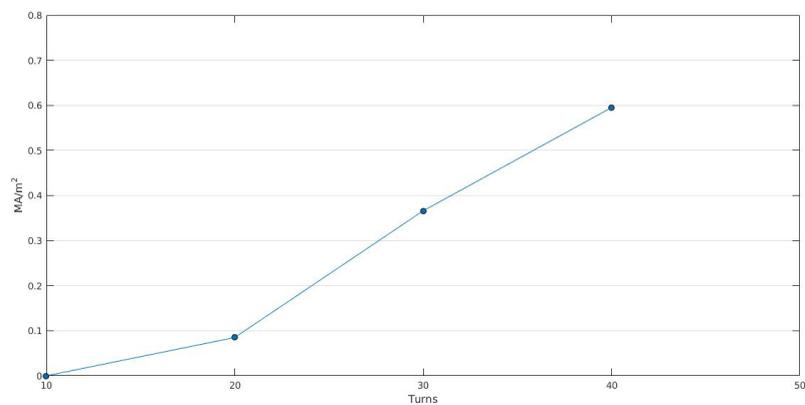Figure 4.20: Data analysis based on Femm simulations

Figure 4.21: central point of the single wire, current density trend over turns

shows that the for higher parallelism the current density decreases. This peculiarity is of utmost importance because it is symptom of the *winding capability to prevent the flux from escaping the torus, that otherwise would increase the losses in the ferrite*. As a matter of fact, comparing the complete view of the inductor with 10 turns (Figure 4.18a) with the one having 40 turns (Figure 4.18b), it is observable that the inductor with a more constant distribution of wires along the circumference tends to confine the flux inside the ferrite region, forming a sort of "magnetic wall" against leakage fluxes. It has also to be underlined that the number of flux lines drawn for the simulation with 40 turns is *three times* the number of the others, otherwise practically no line escaped from the core would have been shown.

This property is not directly related to the Litz wire, cause it is not common practice to unroll a litz wire for covering a surface, but introduces an engineering trade-off. Considering the same toroidal inductor, a more compact set of turns around the core prevents ferrite losses derived from leaked flux, but requires more copper and so a heavier presence of copper losses. On the contrary, less copper means less copper losses, but, especially for less permeable cores where the flux easily tends to leak, windings do not confine flux with the same effectiveness, leading to ferrite losses.

From this analysis it might be stated that, between two equally resistive coils having different number of wires in parallel, the solution with higher parallelism should be chosen, and should moreover present:

- More active copper;

- Less losses;

- More uniform distribution.

As conclusion of this chapter, the total losses measured within the Femm simulations for both toroidal inductors 55735 and T200-2B. These values act as theoretical comparison between toroidal solutions against planar one: therefore, the simulations must comply with the real characteristics of the objects, in order to obtain correct and accurate estimations. For this reasons, a purchasable and feasible litz wire has to be wound around the torus instead of the arbitrary wire chosen for the previous analysis. The chosen nominal conducting surface has been selected as

$$S = 13.8 \text{cm}$$

which under the practical simulation limit of a litz wire made of 4 single insulated wires, yield a radius of

$$r = \sqrt{\frac{13.8}{4 * \pi}} = 1.05 \text{mm}$$

Table 4.3: Numerical comparison between inductor solutions

	Losses
Planar inductor	1.80 W
55735 (Magnetics)	1.24W
T200-2B (Micrometals)	3.17W

which is indeed a purchasable solution.

This value for the copper section of the torus has been selected so to be *equal to the planar copper section* (retrieved from the corresponding Gerber files). In this way, the values obtained from Femm will depend more on the geometrical characteristics of the inductors rather then on the quantity of copper.

The Femm implementation of both inductors in Figure 4.22, where the presence of equally sized boundaries is shown so to appreciate the difference in the dimensions of the two cores, and the green regions are the selection for the loss calculation. Furthermore, the numerical results of all three solution are summed in the table 4.3 .
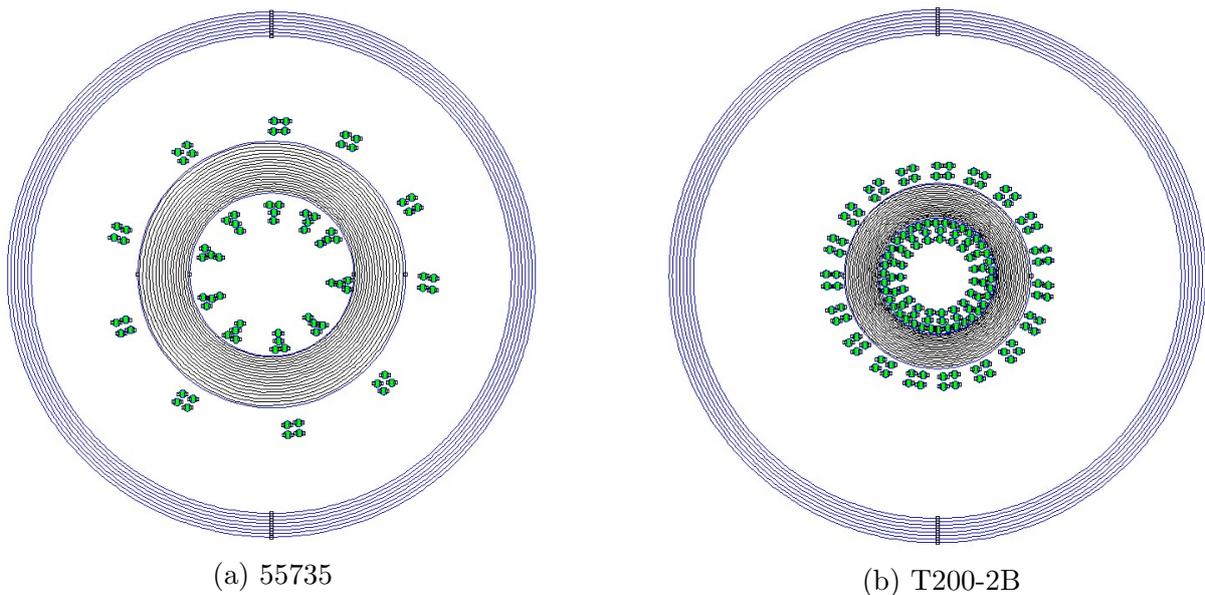

(a) 55735

(b) T200-2B

Figure 4.22: Femm implementation of toroidal inductors for total loss calculation

According to the numerical values, the question of whether the toroidal inductor is more suitable for this converter than a planar one received only half answer. As a matter of fact, although the core from Magnetics outdoes the planar one, the third and cheaper object seems to be unsatisfactory. In the next chapter, practical tests will demonstrate that, for this converter, this is not true.

Chapter 5

Practical results and measurements

This final chapter investigates the results obtained from simulations of the previous chapter by means of experiments on the charger itself, once the different inductors are installed in it.

As long as the work of this thesis is concerned, the chosen core for toroidal solutions might be manufactured by either Magnetics or Micrometals, these two having differences in terms of effectiveness of the product and its implementation. Generally speaking, as obtained from simulations, Magnetics' cores are more efficient and expensive, whereas Micrometals' ones release more heat and are cheaper. Moreover, by looking at the relative tables, it is noticeable that the average number of turns required by Micrometals' cores is more than the ones for Magnetics, this mainly because of the lower permeabilities of the former with respect to the latter, leading to much higher copper losses.

For these experimental chapter, due to economical and engineering evaluations, the torus are from Micrometals. Therefore, the set of measures on the overall efficiencies and power losses of the charger will be described and commented for the planar inductor and for the T200-2B wound with litz wire, leading to the conclusions.

5.1   Introduction to the experiment

This set of measurements investigates the overall performances of the converter while different possible AC inductor are installed on it.

During the final period of this thesis, a whole other set of measurements was performed, so to retrieve information about the behavior of each inductor typology. The intention was to obtain a mathematical analysis of the waveforms by means of an oscilloscope upon which calculate values for active/reactive power, losses, etc. so to have a numerical comparison with the theoretical results obtained from simulations (4.3).

However, this piece-to-piece measure approach was found to be heavily affected by noises and uncertainties, which would have led to non-precise and non-robust analysis. The reasons of this are multiple, but the main problem regarded the working principle

itself of the converter. Without exploring the details of these measurements, the fact of having so different operating levels in a single period led to the need of several sensors and several settings, enhancing errors and noises on the computed waveforms.

The parallel reasoning, upon which this thesis is focused, regards the fact that indeed *the designer has to obtain a good converter rather than a good inductor*. Therefore, the main concern should be on the charger efficiency, which is for sure related to the efficiency of the chosen AC inductor. Therefore, the reasoning of this section will be from an higher point of view, looking at the system in its totality and measuring it.

More in particular, the variables under observation for this set of measures are:

1. **Power**: primary (P_{in}), secondary (P_{out});

2. **Current**: primary (I_{in}), secondary (I_{out});

3. **Voltage**: primary (V_{in}), secondary (V_{out});

4. **Efficiency** μ.

The arrangement for these tests makes use of electrical equipment specifically employed so to be interfaced with both the charger and the other instruments. The main ones, along with their configuration, are:

1. Programmable power supply TDK Lambda DC/DC, connected downstream of the bridge rectifier (not needed for direct DC supply). In fact, an upstream connection would have led to include the bridge fictitious losses in the measures.

2. BK Precision programmable DC electronic load, with maximum current of 12A. Connected to the secondary so to impose a load to the system.

3. Hall effect current sensors by LEM, for both primary and secondary. With a full-scale of 700A, a specific set of windings were employed so to amplify the sensed current, therefore increasing the accuracy of the measures even at the relative low currents of this experiment.

4. Power meter Yokogawa for elaborating the output of the converter. Its input for this set of measurements are voltage and current from both primary and secondary. The additional elaboration consists in calculating the powers P_{in} and P_{out} and the consequent efficiency μ

Although the nominal current provided by the charger and flowing in the batteries under real conditions is 16A, the owned electrical load can reach a maximum of 12A. Therefore, the experiment is aimed to obtain a set of values under different working condition and different inductors installed , so to analyze the behavior **trends** rather then the single values in order to estimate the behavior at nominal conditions. Data are acquired for each combination of the following parameters:
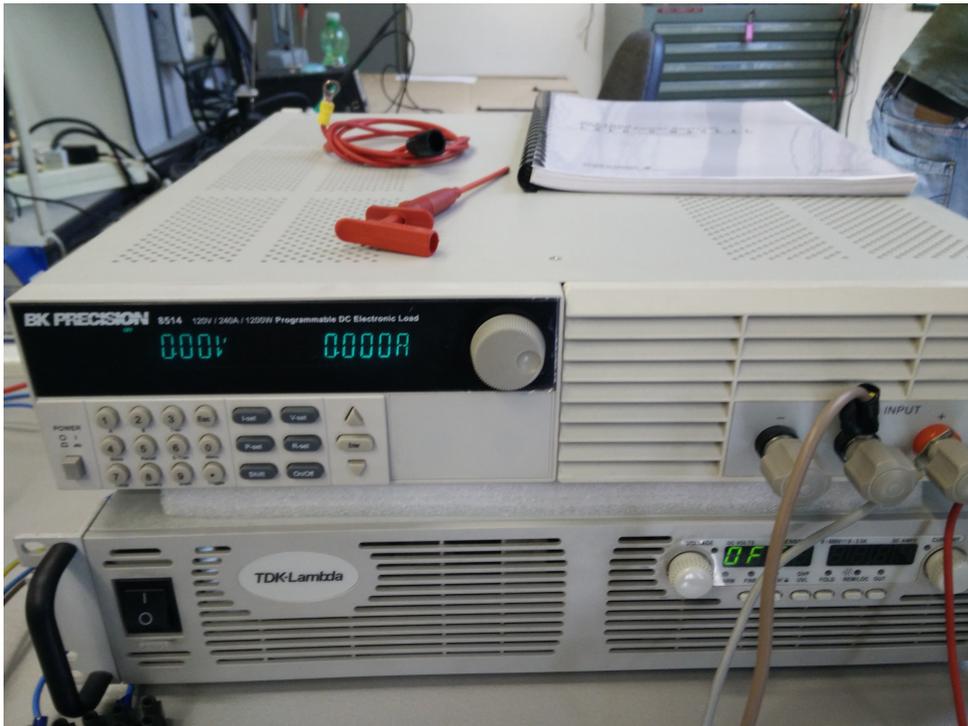
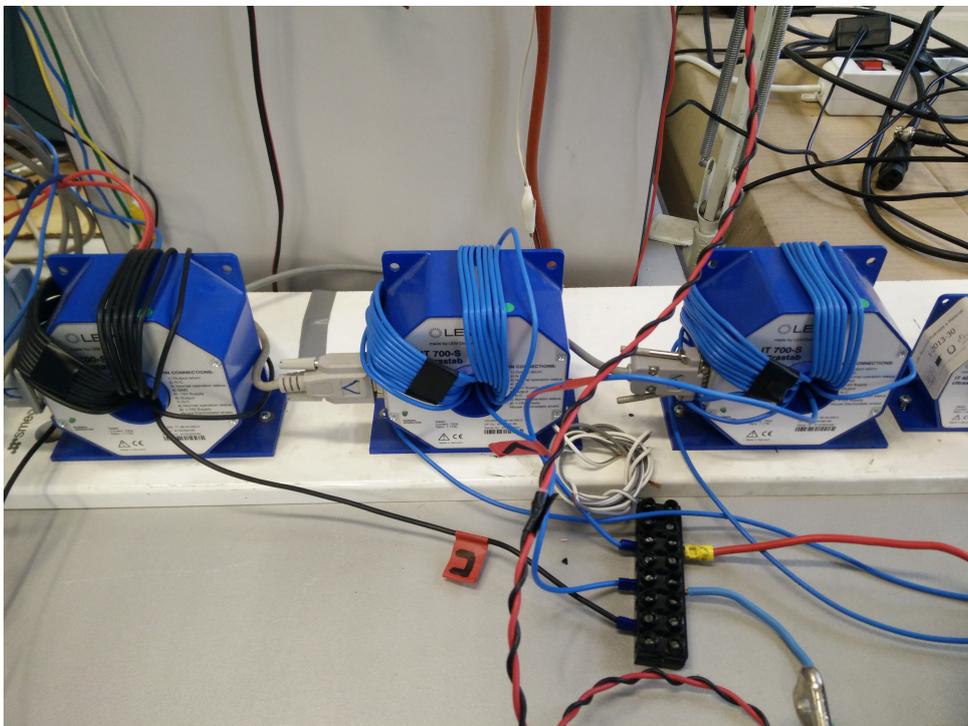Figure 5.1: Electronic load and DC power supply

Figure 5.2: Set of wounded Hall effect current sensors

- Secondary current: 3A, 6A, 9A, 12A;

- Inductor: pcb with planar ferrite, toroidal core with litz wire windings.

Therefore, the total number of acquirement is

$$4(\text{current values}) * 2(\text{inductor types}) = 8$$

.The procedure of the experiment is the following: once the first inductor is correctly welded on the charger board, the voltage to the primary side is slowly brought to the nominal value of 325V by means of the TDK-Lambda. The load now can be set to one of the under-test values by means of the electronic load: this operation forces the controller to operate with a switching timing such that the primary current assumes a value capable of supplying the secondary with the imposed power. Therefore, the more current is necessary at the primary side, the more losses are present in the circuit. As a matter of fact, the efficiency is calculated based on the ratio between P_{out} and P_{in}. Meanwhile, the power-meter samples voltages, currents and calculates the corresponding powers and efficiency. The data acquirement should happen only after the transitory period, under steady state conditions. This process is repeated first varying the current, then from the very beginning with the other inductor.

The expected situation is that, for the same I_{out} with different AC inductors welded, P_{out} measured by the power-meter are approximately the same. If this was not true, a comparison between different inductor typologies would require different kinds of measures.

5.2   Results and comment

The confirmation of the hypothesis for the experiment, as well as the proof of effectiveness of the toroidal solution comes from the resulting data, tabled in 5.1.

Set Iout(A)	Vin (V)	Iin (A)	Pin (kW)	Vout (V)	Iout (A)	Pout (kW)	efficiency (%)
pcb							
3	324,44	1,3966	0,453	132,86	3,019	0,4011	88,518
6	324,19	2,6779	0,8681	132,81	6,015	0,7989	92,022
9	323,92	3,9819	1,2898	132,75	9,016	1,1968	92,791
12	323,64	5,286	1,7106	132,66	12,023	1,595	93,24
torus							
3	324,52	1,3777	0,447	132,87	3,0218	0,4015	89,8
6	324,25	2,653	0,8603	132,81	6,017	0,7991	92,89
9	323,98	3,9549	1,2813	132,76	9,02	1,1975	93,46
12	323,7	5,243	1,6973	132,69	12,029	1,5961	94,035

Table 5.1: Acquired data

The equality condition of the power at secondary is satisfied, meaning that

$$P^i_{out_{pcb}} \approx P^i_{out_{torus}} \forall i \in \{3, 6, 9, 12\}$$

Moreover, looking at the other results in the table, the V_{in} as expected is almost constant throughout the whole experiment, being it externally supplied. The same applies to V_{out}, being it directly controlled by the controller. $I_{out} \approx SetI_{out}$ act as sort of feedback for ensuring the correct functioning of the system.

Apart from the efficiencies already calculated by the power-meter, the comparison between pcb and Torus is indeed accomplished by calculations based on the previous data. The quantities of interest are:

- P_{lost} calculated as

$$P_{lost} = (P_{in} - P_{out}) * 1000$$

which is indeed the power dissipated as heat by the converter during its operations. The multiplication accounts for the transformation from KiloWatts to Watts.

- ΔP_{in} calculated as

$$\Delta P_{in} = P_{in_{pcb}} - P_{in_{torus}}$$

When positive, it represents the power saved by choosing a toroidal inductor rather than a pcb-based one.

- $\Delta P^{\%}_{in}$ calculated as

$$\Delta P^{\%}_{in} = \frac{\Delta P_{in}}{P_{in_{pcb}}} * 100$$

When positive, it represents the percentage of power saved by choosing the toroidal solution with respect to the power needed with the pcb installed.

The numerical values obtained from these calculation are reported in the Table 5.2. The

Set Iout(A)	Plost pcb	Plost torus	ΔPin	ΔPin%
3	51,9	45,5	6,4	12,33
6	69,2	61,2	8	11,56
9	93	83,8	9,2	9,89
12	115,6	101,2	14,4	12,46

Table 5.2: Data comparison between pcb and torus

fact that

$$\Delta P_{in} > 0$$

and consequently also $\Delta P^{\%}_{in}$ is positive, proves Q.E.D. that *the charger performs better with the toroidal inductor rather than the planar one, which implicitly confirms the*

improvements predicted by means of theoretical analysis and simulations long the whole thesis.

However, the real aim of these measures was not the pursue of a numerical proof of improvement, but rather a trend analysis of the charger behavior in different conditions, being the real load of the charger different from the imposed one. The nominal current at the secondary for the longest recharging period of the batteries is $I_{out} = 16A$, that was not possible to be simulated in the lab. The best way for appreciating a trend is by means of plots. The quantities to be analyzed are efficiencies and difference in power consumption, both in absolute and relative terms, which respectively leads to plot η_{torus} and η_{pcb} (Figure 5.3), ΔP_{in} (Figure 5.4) and $\Delta P_{in}^{\%}$ (Figure 5.5).
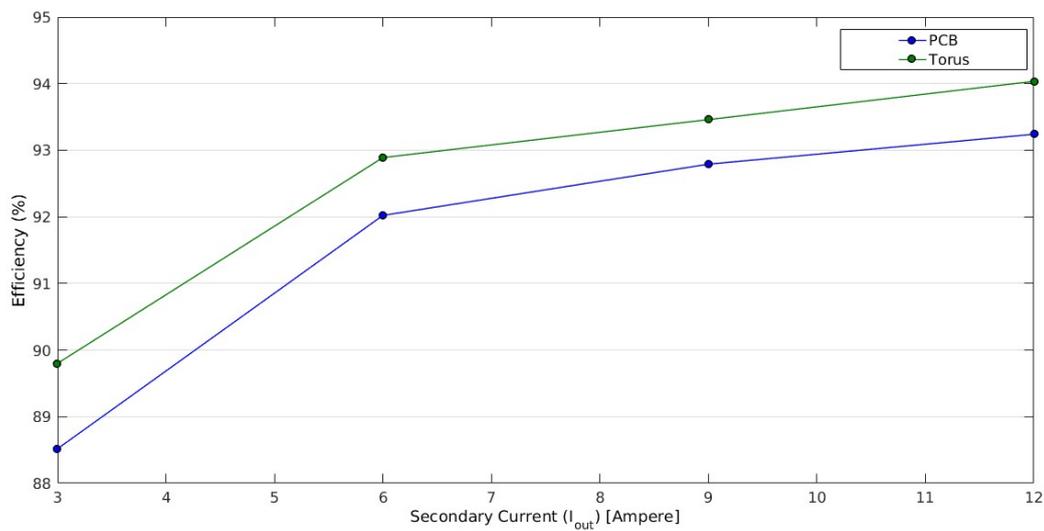

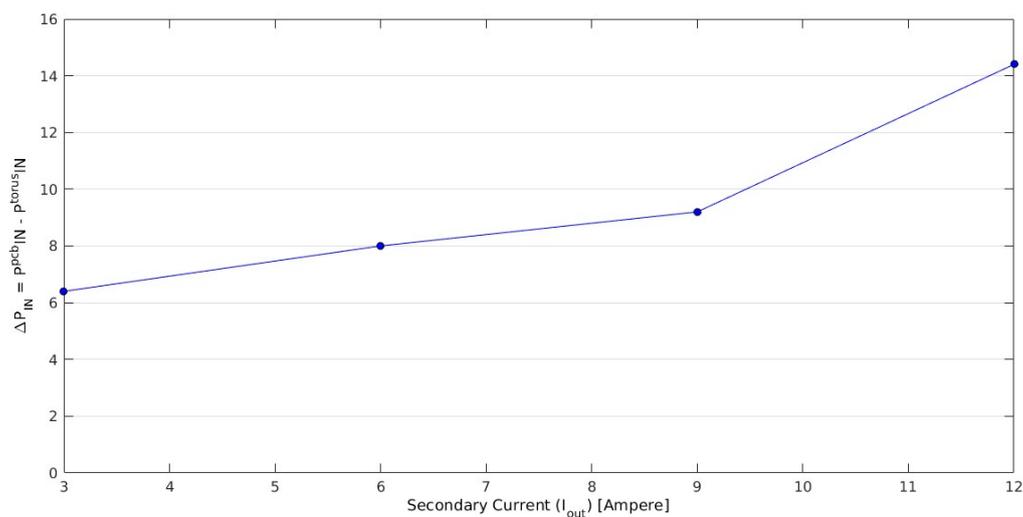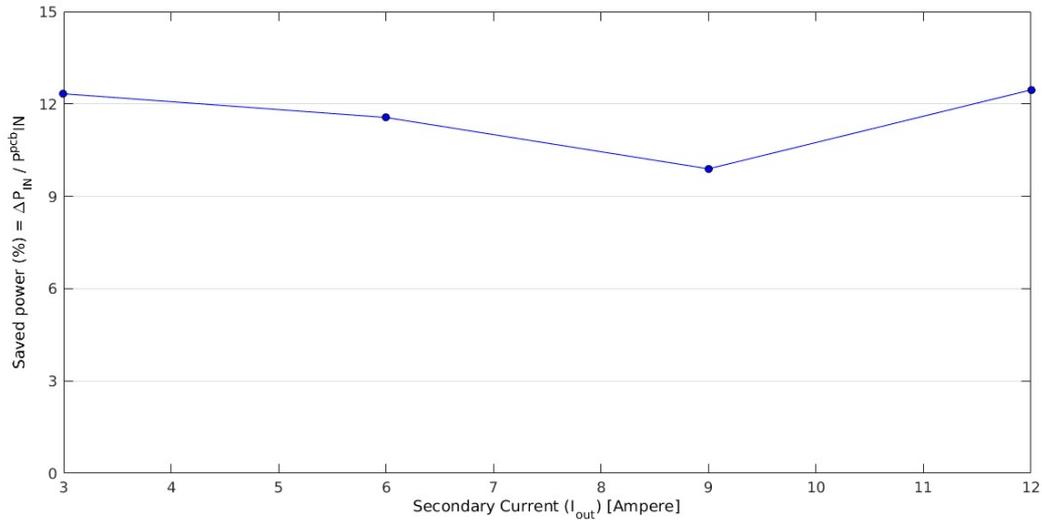Figure 5.3: η_{torus} and η_{pcb} in comparison

Figure 5.4: ΔP_{in}

From the efficiency plot, an almost constant improvement of $\Delta \eta \approx 1 - 1.5\%$ is visible for each of the four acquirements, pointing out that this sort of benefit is likely to be

Figure 5.5: $\Delta P_{in}^{\%}$

present even at $I_{out} = 16$A. It is interesting to notice the positive slope of both graphs, which indeed confirms the fact that this converter performs better with bigger load rather than smaller, mainly due to ZVS conditions as discussed in Chapter 1.

The astonishing result regards the saved power that goes along with this $1 - 1.5\%$ efficiency improvement. In absolute terms, a constantly increasing saved power results from an increasing load, which is not surprising as long as the load increases. In relative terms, however, the Figure 5.5 shows an almost constant $11 - 12\%$ **saved power** with respect to the one needed by the pcb. This almost steady curve suggests the likelihood of a similar percentage for the nominal condition, beside reporting that just by changing one single component of the converted the obtained improvement is substantial. This result is an evidence of the key and cumbersome role played by the AC inductor in this kind of converter.

Chapter 6

Conclusions

After a first introduction in Chapter 1 about the functioning of the charger itself, along with a general overview regarding the issues that have to be faced at high frequencies with magnetic and conductive materials (Chapter 2), the comparison between planar inductor (Chapter 3) and toroidal inductor (Chapter 4) has been faced. More in particular, a deeper analysis of the magnetism in ferromagnetic materials allowed the design of a toroidal inductor aimed to outdo the planar one in terms on efficiency and power loss. After theoretical discussion and simulation, indeed the measurements proved the thesis of this paper (Chapter 5).

Further and suggested experiments are thermal tests on both solutions once they are installed on the converter, so to ensure the thermic stability before definitive installation.

Bibliography

[1] V. Giammarino, "Design of the transformer of a zvs phase-shifted dc/dc power converter for automotive applications," 2016.

[2] S. Lombardi, "convertitore switching ad alta frequenza per batterie al litio," 2015.

[3] Magnetics, "Official magnetics website, front page." `https://www.mag-inc.com/`.

[4] Magnetics, "Learn more about powder cores." `https://www.mag-inc.com/products/powder-cores/learn-more-about-powder-cores`, 2016.

[5] Magnetics, "Magnetic powder core catalog." `http://www.micrometals.com/whatwedo_index.html`, 2015.

[6] Micrometals, "Design tool by micrometals." `http://www.micrometals.com/software_index.html`, 2010.

[7] Micrometals, "About micrometals." `http://www.micrometals.com/whatwedo_index.html`, 2016.

[8] Micrometals, "Power conversion & line filter applications catalog." `http://www.micrometals.com/pcparts/PC_L.pdf`, 2016.